Induced polarization images alteration in stratovolcanoes

André Revil, Youzheng Qi, Neha Panwar, Marceau Gresse, Hendra Grandis, Ravi Sharma, Yves Géraud, Nadjib Chibati, Ahmad Ghorbani

Journal of Volcanology and Geothermal Research 429 (2022) 107598

Contents lists available at ScienceDirect

Journal of Volcanology and Geothermal Research

journal homepage: www.journals.elsevier.com/journal-of-volcanology-and-geothermal-research

Induced polarization images alteration in stratovolcanoes

A. Revil [a,*], Y. Qi [a], N. Panwar [a,b], M. Gresse [c], H. Grandis [d], R. Sharma [b], Y. Géraud [e], N. Chibati [e], A. Ghorbani [f]

[a] Université Grenoble Alpes, Univ. Savoie Mont-Blanc, CNRS, UMR CNRS 5204, EDYTEM, Le Bourget du Lac, France
[b] Indian Institute of Technology, Roorkee, Uttarakhand, India
[c] Research Institute of Earthquake and Volcano Geology, Geological Survey of Japan, AIST, Tsukuba, Japan
[d] Faculty of Mining and Petroleum Engineering, Institut Teknologi Bandung, Jalan Ganesha 10, Bandung, Indonesia
[e] Université de Lorraine, CNRS, GeoRessources, F-54000 Nancy, France
[f] Yazd University, Department of Mining and Metallurgical Engineering, Yazd, Iran

ARTICLE INFO

Keywords:
Electrical conductivity
Electrical properties
Hydrothermal systems
Resistivity tomography (ERT)
Induced polarization

ABSTRACT

We investigate the complex conductivity of 32 volcanic rock samples from two stratovolcanoes, La Soufrière Volcano (Guadeloupe Island, Caribbean) and Papandayan volcano (Java Island, Indonesia). These stratovolcanoes are characterized by high degrees of kaolinite-related alteration associated with the upwelling of acidic ground waters as well as the formation of smectite-rich clay caps. Our goal is to assess the dependence of two geoelectrical properties, the electrical conductivity and normalized chargeability, on the conductivity of the pore water and the Cation Exchange Capacity (CEC) for volcanic rocks at near-neutral pH conditions. An alteration index based on CEC is built for both smectite- and kaolinite-rich zones. The data are discussed in the context of a previously acquired experimental dataset based on samples collected from shield volcanoes in Hawaii. We show that all the core samples display the same trends in their petrophysical geoelectrical properties whatever the type of volcanoes. Surface conductivity and normalized chargeability are strongly controlled by the CEC of the material and the bulk tortuosity of the pore space (product of the formation factor by the porosity). This implies in turn that the conductivity and the normalized chargeability are controlled by rock alteration in the same way as long as surface conductivity dominates the bulk conductivity contribution, which is salinity and pH dependent (both being interrelated in acidic pore waters). These petrophysical results are then applied to the interpretation of a 3D induced polarization survey performed at Papandayan stratovolcano in Indonesia. The tomograms are used to image the alteration of the volcanic edifice and we conclude that surface conduction is non-negligible in these volcanoes. Only above a pore water conductivity higher than 10 S m^{-1} at 25 °C) the bulk conductivity dominates the surface conductivity associated with alteration.

1. Introduction

Stratovolcanoes form dangerous and mechanically unstable edifices, which can release high amounts of ashes and generate pyroclastic flows. The collapse of their flanks can be triggered by several mechanisms including pore-fluid pressurization associated with differential thermal expansions between the fluid and solid phases and forced fluid injection (Reid, 2004; Ball et al., 2018). The mechanical weakening of a stratovolcano can be caused not only by the presence of cracks and faults but also by the alteration of the rocks associated with acidic ground waters (Watt et al., 2012; Watters et al., 2000; Salaun et al., 2011).

Numerous alteration paths and forms may co-exist in a volcanic edifice. In the present paper, we use the word alteration in a restrictive sense which is the following: Alteration denotes the replacement of primary minerals (usually silicates) by secondary mineral assemblages containing some clay minerals and zeolites. An alteration index can be defined as for instance in Revil et al. (2020). Of course, there are other alteration minerals and complex mixtures of these minerals can exist in hydrothermal environments. That said, it should be remembered that only clay minerals (and especially smectite because of its large cation

* Corresponding author.
E-mail addresses: andre.revil@univ-smb.fr (A. Revil), uzhengqi@gmail.com (Y. Qi), npanwar@es.iitr.ac.in (N. Panwar), marceau.gresse@gmail.com (M. Gresse), grandis@geoph.itb.ac.id (H. Grandis), ravi.sharma@es.iitr.ac.in (R. Sharma), yves.geraud@univ-lorraine.fr (Y. Géraud), nadjib.chibati@univ-lorraine.fr (N. Chibati), aghorbani@yazd.ac.ir (A. Ghorbani).

https://doi.org/10.1016/j.jvolgeores.2022.107598
Received 7 October 2021; Received in revised form 18 May 2022; Accepted 4 June 2022
Available online 9 June 2022

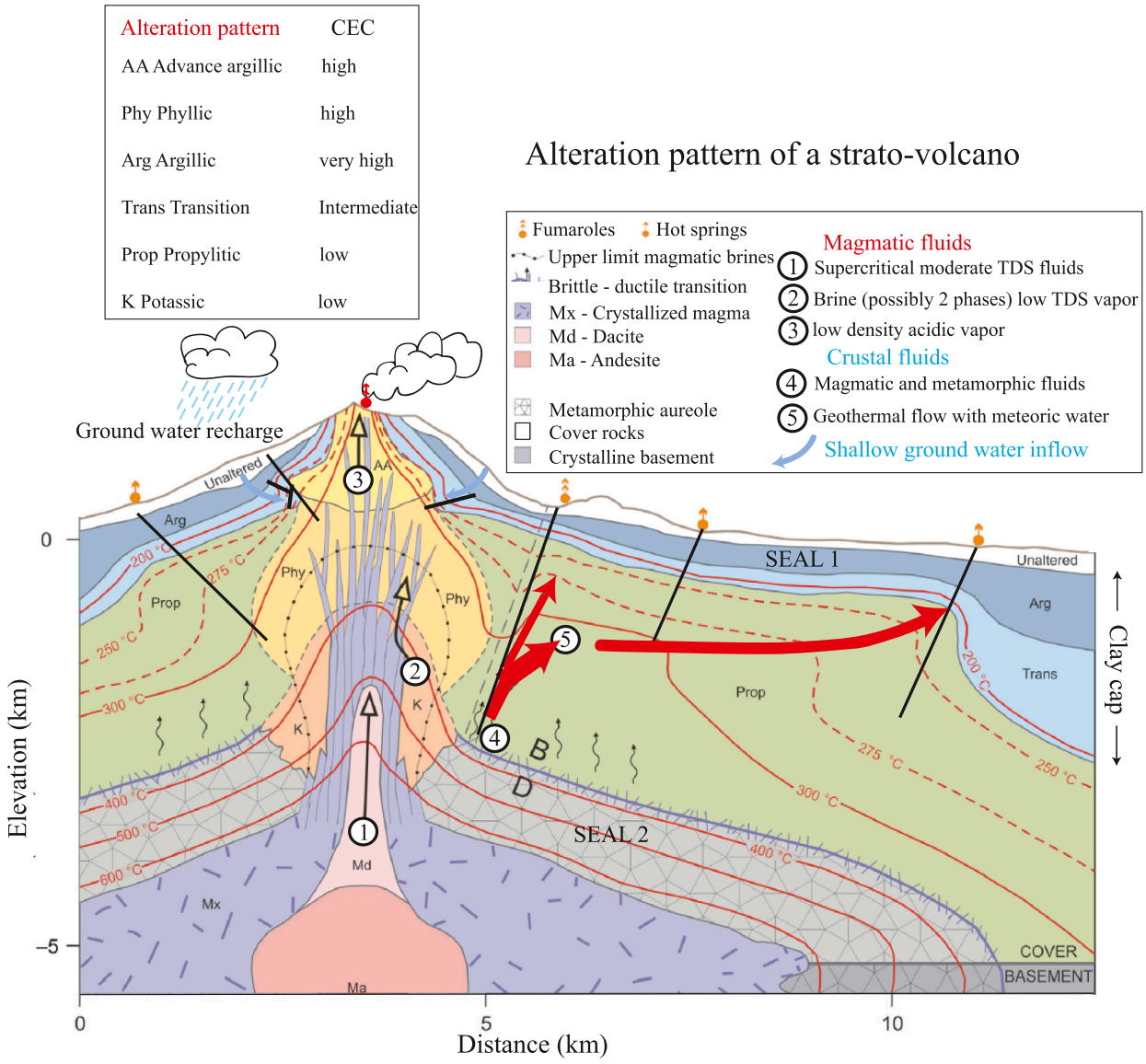

Fig. 1. Distribution of the alteration minerals in a stratovolcano. Adapted from Richard (2011) and Stimac et al. (2015). Induced polarization can be used to decipher the alteration pattern in such an environment, which has implication regarding the mechanical stability of these volcanic edifices and phreatic and phreatomagmatic eruptions. SEAL1 corresponds to the smectite-rich clay cap. The shallow water table is located above this layer. SEAL2 corresponds to the permeability barrier associated with the brittle-ductile transition zone around the magmatic body. CEC stands for Cation Exchange Capacity.

exchange capacity) and semi-conductors (pyrite and magnetite) can influence the geoelectrical properties of the volcanic rocks (mostly basaltic andesites, pyroxene andesites, and pyroxene dacites) investigated in this study.

Alteration also form smectite-rich sealing caps trapping ascending magmatic gases, which can eventually result in overpressuring and sudden explosive eruptions during unrest (e.g. Mannen et al., 2019). Tsunamigenic landslides and avalanches are also often observed on volcanic islands with stratovolcanoes because of flank collapses (López and Williams, 1993; Janssen et al., 2002; Hadisantono, 2006; Sassa et al., 2016). It follows that these volcanic edifices represent strong geohazards that need to be assessed from different perspectives including geophysical imaging and monitoring (Finn et al., 2001; Carracedo and Troll, 2013).

Induced polarization is a geophysical method initially developed in the realm of ore prospection (Schlumberger, 1920; Revil et al., 2022) and used later in the field of environmental geophysics and biohydrogeophysics (e.g., Abdel Aal and Atekwana, 2014; Binley et al., 2015; Flores Orozco et al., 2015). It extends the classical electrical conductivity method (Schmutz et al., 2000; Finizola et al., 2006; Johnson et al., 2010) by including the study of the reversible accumulation of electrical charges under an applied (external) electrical field (Lyklema, 2002; Titov et al., 2002; Leroy et al., 2008). This reversible charge carrier accumulation is called (low-frequency) induced polarization in geophysics, impedance spectroscopy in material sciences, and low-frequency dielectric spectroscopy in colloidal sciences (e.g. Lyklema, 2002; Lesmes and Morgan, 2001). That said, it should be remembered that the underlying physics is distinct from dielectric polarization mechanisms that can be observed at higher frequencies (typically >10 kHz) including the Maxwell-Wagner (interfacial) polarization and dielectric polarization per se. Low-frequency induced polarization is due to the fact that the charge carriers are controlled by electrochemical potential gradients rather than by the Coulombic field alone (Lyklema, 2002). The accumulation of charge carriers occurs at some polarization length scales such as pore or grain scales (Niu et al., 2016). Such a galvanometric method can be used to image at the scale of few kilometers (Gross et al., 2021). It complements electromagnetic methods classically used in geothermal exploration (Muñoz et al.,

a. La Soufrière core samples

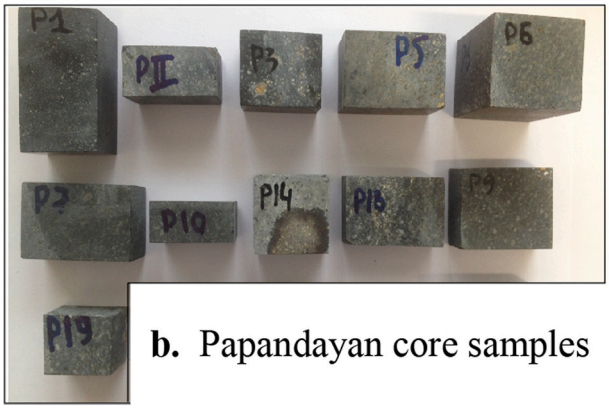

b. Papandayan core samples

Fig. 2. Core samples, impedance meter, and position of the electrodes on the sample holders. a. Core samples from La Soufrière volcano with their insulating tape around them. The saturations are done under vacuum (below 1 mbar). Samples #1, 2, and 9 are fractured. b. Consolidated core samples from Papandayan volcano (see Ghorbani et al., 2018). The average length and width of the cubic samples from Papandayan are 5 and 2.5 cm, respectively. The protocol used for the unconsolidated samples is the same as in Revil et al. (2017c).

2010a, 2010b; Muñoz, 2014). In addition, these methods can come as a complementary source of information to seismological data in order to decipher the complex geometry of active volcanoes and to monitor their hydrothermal systems (Liotta et al., 2020).

Revil et al. (2017a, 2017b) and Revil et al. (2019) developed a petrophysical model able to explain and predict both the electrical conductivity and induced polarization properties of volcanic rocks with a special focus on the basaltic rocks from shield volcanoes. In these volcanoes, the pore waters are characterized by neutral to basic pH values (in some specific cases, the pore water can be however locally acidic). Gross et al. (2021) developed a large-scale induced polarization method to image volcanoes extending previous works done by Johnson et al. (2010) and Soueid Ahmed et al. (2018) regarding the development of tomographic algorithms accounting for rough topographies. Revil et al. (2021) demonstrated how induced polarization could be used to image the temperature field of shield volcanoes with an application to Kilauea in Hawaii. Revil et al. (2019) characterized clay caps in geothermal fields using this method.

In the present paper, we study 10 new core samples from La Soufrière volcano, an andesitic stratovolcano located south of Basse-Terre Island, Guadeloupe archipelago, in the Caribbean. This volcano is an active edifice with fumaroles and gas emissions and active hydrothermal manifestations and production of the different products (lava, ashes, pyroclastic materials). The development of this specific volcano is affected by several phases of flank instabilities, with landslides and debris avalanche (Samper et al., 2009). These samples are saturated at three pore water salinities (NaCl solutions). In addition, we reuse 22 samples from Papandayan volcano, an andesitic stratovolcano located in Java Island in Indonesia (see Ghorbani et al., 2018). These new data are compared to published measurements made with core samples from shield volcanoes in Hawaii (Revil et al., 2021). All the core samples have been selected to cover a broad range of porosity and alteration states in order to decipher their influence on the complex conductivity spectra. Then, the resulting experimental results are used to interpret a new field induced polarization survey acquired at Papandayan stratovolcano. Papandayan (2665 masl, meters above sea level) is the southern-most volcano of Western Java Island. This volcano is characterized by an intense hydrothermal activity, which is evidenced by both fumaroles and gas emissions, sulfate mud pools, and four active vents called the Mas, Manuk, Nangklak, and Baru craters. Hydrothermal alteration makes this edifice gravitationally unstable and prone to landslides, debris avalanches, and possibly flank collapses. Therefore characterizing the hydrothermal system and estimating the spatial distribution and strength of alteration is important to better assess volcanic hazards. In the last decade, geophysical imaging methods such as passive seismic, magnetotelluric, and electrical resistivity have been used at Papandayan (Triastuty et al., 2006; Nasution et al., 2008; Nurhasan et al., 2012; Byrdina et al., 2018). However, to date, none of these geophysical methods could be used to quantitatively assess the intensity of supergene to advanced argillic alteration in stratovolcanoes.

2. Background on induced polarization

2.1. Petrophysical model

We assume a time-invariant, linear, isotropic volcanic rock. At low frequencies, Ohm's law between the current total density J (in A m^{-2}) and the applied electrical field E (in V m^{-1}) is given by (Revil et al., 2017a, 2017b),

$$\mathbf{J} = \sigma^*(\omega)\mathbf{E} \tag{1}$$

$$\sigma^*(\omega) = \sigma'(\omega) + i\sigma''(\omega) \tag{2}$$

$$\sigma^*(\omega) = \sigma_\infty - M_n \int_0^\infty \frac{h(\tau)}{1+(i\omega\tau)^{1/2}} d\tau \tag{3}$$

where i denotes the pure imaginary number ($i^2 = -1$), σ^* denotes the complex-valued electrical conductivity (S m^{-1}), ω is the angular frequency (rad s^{-1}), M_n (S m^{-1}) denotes the normalized chargeability, τ (in s) is a (relaxation) time constant, and $h(\tau)$ denotes a (normalized) probability density for the distribution of the (relaxation) time constants of the material. The real part of the complex conductivity (called the in-phase conductivity below), σ' (>0, in S m^{-1}) characterizes the process of conduction (i.e., the electromigration of the charge carriers in response to the imposed electrical field). The imaginary part of the complex conductivity σ'' (<0, named quadrature conductivity and expressed in S m^{-1}) characterizes polarization, i.e. the reversible accumulation of charge carriers in response to the imposed electrical field (Olhoeft, 1985; Börner et al., 1993). At first approximation, each element of a volcanic edifice can be considered as a resistance in parallel to a capacitance and an equivalent electrical circuit can be used to assess the electrical properties of a rock.

In absence of semi-conductors, the normalized chargeability and instantaneous conductivity are given by (Revil et al., 2017a, 2017b),

$$M_n = \theta^{m-1}\rho_g \lambda \mathrm{CEC} \tag{4}$$

Table 1
Properties of the samples. Samples S1 to S10 belongs to la Soufrière volcano. Samples S11 to S32 belongs to Papandayan. The pH is the equilibrium pH of the solution for the cation exchange capacity measurements. Note that the pH of the solution in equilibrium with the core samples varies from neutral from strongly acidic, an expected results for stratovolcanoes. The quantity S_{sp} denotes the specific surface area of the core samples. A qualitative description of the rock samples is: CR: consolidated volcanic rocks from outcrops, UR: unconsolidated volcanic rocks taken from outcrops, FL: Fresh lava, SMDF: Poorly altered debris flow, HDF: strongly altered debris flow, FDF: Fresh debris flow, and SML: Poorly altered lava. The CEC is expressed in meq/100 g (1 meq/100 g = 963.20C kg^{-1} in SI units). The samples from Papadayan are rather fresh andesites.

Sample ID	Full name	Description	Porosity ϕ (−)	CEC (meq/100 g)	pH (−)	S_{sp} BET (m^2/g)	ρ_g (kg/m^3)
S1	GD15–15-2	FL	0.011	2.58	7.06	27.1	2923
S2	GD15–165	FL	0.04	0.65	7.49	6.0	2834
S3	GD15–03	SMDF	0.29	8.72	6.68	122	2899
S4	GD16–24	HDF	0.30	17.41	6.33	235	2921
S5	GD16–09	FDF	0.31	17.41	6.28	212	2911
S6	GD16–26	FDF	0.39	8.62	5.09	89.9	2896
S7	GD15–10-2	FDF	0.33	11.84	3.71	152	2921
S8	GD15–15S	FDF	0.34	17.53	7.68	85	2845
S9	GD15–160	FL	0.116	1.29	7.32	12.5	2833
S10	GD15–150	SML	0.27	3.95	6.53	58.2	2895
S11	P1	CR	0.022(1)	1.2(1)	7.18(1)	18.3	2759(1)
S12	P2	CR	0.031(1)	4.7(1)	6.18(1)	67.9	2551(1)
S13	P3	CR	0.032(1)	4.5(1)	7.14(1)	51.2	2707(1)
S14	P5	CR	0.038(1)	3.4(1)	5.37(1)	48.9	2681(1)
S15	P6	CR	0.044(1)	1.6(1)	5.15(1)	21.1	2700(1)
S16	P7	CR	0.030(1)	1.3(1)	6.54(1)	5.9	2789(1)
S17	P8	CR	0.032(1)	4.1(1)	8.02(1)	67.0	2706(1)
S19	P9	CR	0.037(1)	1.6(1)	4.13(1)	22.1	2863(1)
S20	P10	CR	0.037(1)	1.6(1)	6.25(1)	22.1	2684(1)
S21	P14	CR	0.057(1)	1.3(1)	5.36(1)	16.9	2737(1)
S22	P18	CR	0.056(1)	1.3(1)	7.11(1)	16.9	2824(1)
S23	P19	CR	0.030(1)	–	–	–	2815(1)
S24	PN1	UR	0.71(1)	2.4(1)	3.31(1)	45.3(1)	2847
S25	PN2	UR	0.65(1)	5.1(1)	5.54(1)	33.3(1)	2903
S26	PN3	UR	0.70(1)	3.9(1)	4.21(1)	102.8(1)	2799-
S27	PN4	UR	0.63(1)	1.38(1)	3.40(1)	34.7(1)	2921
S28	PN6	UR	0.72(1)	5.7(1)	2.43(1)	7.4(1)	2812
S29	PN7	UR	0.65(1)	2.3(1)	3.24(1)	29.4(1)	2846
S30	PN8	UR	0.69(1)	2.3(1)	2.90(1)	51.3(1)	2865
S31	PN9	UR	0.58(1)	0.71(1)	2.40(1)	25.7(1)	2811
S32	PN10	UR	0.62(1)	1.1(1)	3.29(1)	21.6(1)	2899

(1) From Ghorbani et al. (2018)

$$\sigma_\infty = \theta^m \sigma_w + \theta^{m-1} \rho_g B \mathrm{CEC} \tag{5}$$

where $m \geq 1$ (dimensionless) is called the (first) Archie's exponent of Archie's law (see Archie, 1942, typical values of m are around 2.0 ± 0.5) and θ (dimensionless) denotes the water content (product of the porosity ϕ by the saturation s_w) of the liquid water phase, σ_w (in S m^{-1}) denotes the pore water conductivity, ρ_g is the grain density (in kg m^{-3}, typically $\rho_g \sim 2900$ kg m^{-3} for volcanic rocks without metallic particles), CEC denotes the cation exchange capacity of the rock (1 meq g^{-1} = 1 mol kg^{-1} = 96,320C kg^{-1}), B (in m^{2}V^{-1} s^{-1}) denotes the apparent mobility of the counterions for surface conduction (Waxman and Smits, 1968), and λ (in m^{2}V^{-1} s^{-1}) denotes the apparent mobility of the counterions for the polarization associated with the quadrature conductivity and normalized chargeability (Vinegar and Waxman, 1984). In saturated conditions, the conductivity equation can be written as

$$\sigma_\infty = \frac{1}{F}\sigma_w + \sigma_S \tag{6}$$

$$\sigma_S = \frac{1}{F\phi}\rho_g B \mathrm{CEC} \tag{7}$$

$$F = \phi^{-m} \tag{8}$$

where σ_S denotes the surface conductivity and Eq. (8) corresponds to the first Archie's law. The quantity σ_w/F denotes the bulk conductivity associated with conduction in the bulk pore space.

2.2. Fitting model

In order to fit the complex conductivity spectra, we need to replace eq. (3) by a simplified form called a Cole Cole parametric model. In addition, we need to add a second Cole Cole model to represent another polarization mechanism that occurs at higher frequencies and named the Maxwell-Wagner polarization. We will use index 1 to denote the polarization mechanism associated with the polarization of the electrical double layer associated with the insulating grains while the second mechanism (mechanism 2) would correspond to the Maxwell-Wagner polarization. The expression for the effective complex conductivity of a volcanic rock is written as

$$\sigma^* \approx \sigma_\infty \left(1 - \frac{M_1}{1 + (i\omega\tau_1)^{c_1}} - \frac{M_2}{1 + (i\omega\tau_2)^{c_2}} \right) \tag{9}$$

$$M = \frac{\sigma_\infty - \sigma_0}{\sigma_\infty} = M_1 + M_2 \tag{10}$$

$$\sigma_0 = \sigma_\infty (1 - M_1 - M_2) \tag{11}$$

and where M_1 and M_2 are the chargeabilities (dimensionless), c_1 and c_2 are the two Cole-Cole exponents (dimensionless), and τ_1 and τ_2 are the (relaxation) time constants (expressed in s).

The inversion of the spectra can be done with a Bayesian technique (Ghorbani et al., 2018). To invert the 6 unknown parameters of the double Cole Cole model, we use here a Markov Chain Monte Carlo sampling algorithm. The prior information we have on the model vector $\mathbf{m} = [\log(\sigma_0); M_1; \mathrm{logit}(c_1), \log(\tau_1); M_2; \mathrm{logit}(c_2); \log(\tau_2)]$ is described with a probability density P(m). We note $\mathbf{d}_{obs}$ (measured in phase and quadrature conductivity spectra with Gaussian uncertainties) the

Table 2
Samples of the three main facies were selected, lavas, debris flows and pyroclastics. They show three degrees of hydrothermal alteration, healthy (fresh) samples, weakly altered samples, and strongly altered samples. The main primary minerals are plagioclase, pyroxene and magnetite. Secondary minerals precipitated during hydrothermal alteration are clays, pyrite, quartz (Navelot, 2018). The magnetic susceptibility χ is can be used as a proxy for the magnetite content. The primary and secondary minerals are identified than to XRD data and thin section analysis (Navelot, 2018).

Sample ID	Full name	Rock type	Primary minerals	Secondary minerals	χ (10^{-3} S.I.)
S3	GD15–03	SHDF	Plagioclase, magnetite, clinopyroxene, orthopyroxene,	Clay pyrite, iron-oxide quartz	18.37
S4	GD16–24	HDF	–	Clay, iron-oxide, quartz	−0.11
S5	GD16–09	FDF	Plagioclase, magnetite, clinopyroxene, orthopyroxene, amphibole	–	15.73
S6	GD16–26	FP	Plagioclase, magnetite, amphibole, clinopyroxene, orthopyroxene	Clay	12.83
S7	GD15–10	FDF	Plagioclase, magnetite, clinopyroxene, orthopyroxene, quartz	Iron-oxide, clay	6.13
S8	GD15–15	FP	Plagioclase, magnetite, clinopyroxene, orthopyroxene,	–	14.03
S9	GD15–160	FL	Plagioclase, orthoclase, magnetite, clinopyroxene, orthopyroxene	–	6.68
S10	GD15–150	SML	Plagioclase, orthoclase, magnetite, clinopyroxene, orthopyroxene	Iron-oxide, clay	3.58

observed data vector. The posterior probability density σ(m) is given by,

$$\sigma(\mathbf{m}) = kP(\mathbf{m})L(\mathbf{m}) \tag{12}$$

where k is a normalization constant and the likelihood function describing the experimental uncertainties is given by:

$$\mathrm{L(m)} = \mathrm{k} \bullet exp\left[-\frac{\mathrm{S(m)}}{\mathrm{s^2}}\right] \tag{13}$$

where s^2 is the total noise variance (s^2 is the same for all the data, 10%) and where the misfit function $S(\mathbf{m})$ is given by.

$$\mathrm{S(m)} = \frac{1}{2}\sum_{\mathrm{i=1}}^{\mathrm{n}}\left(\mathrm{g^i(m)} - \mathrm{d^i_{obs}}\right)^2 \tag{14}$$

where d is data vector, g(m) is the forward modeling function used to predict the in-phase and quadrature conductivity spectra through the Double Cole Cole model (Eqs. (9) to (11)). The acceptance probability of a new model is

$$\mathrm{P_{accept}}\begin{cases} 1 \mathrm{if} \mathrm{S(m_{new})} \le \mathrm{S(m_{old})} \\ exp\left(-\frac{\Delta \mathrm{S}}{\mathrm{s^2}}\right) \mathrm{if} \mathrm{S(m_{new})} \rangle \mathrm{S(m_{old})} \end{cases} \tag{15}$$

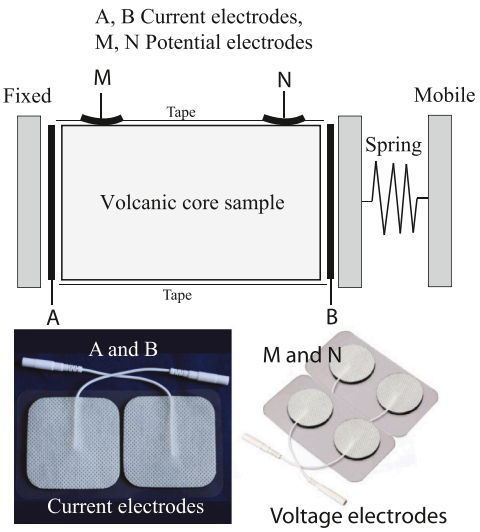

Fig. 3. Sketch of the experimental setup for the consolidated volcanic core samples. The electrodes are self-adhesive super conductive carbon film, carbon/Ag/AgCl electrodes with biocompatible hydrogel. We did not use metallic pieces in order to minimize spurious polarization effects. The electrodes are removed from the core samples after the measurements. The conductive gel insures a uniform contact between the electrodes and the core sample that does not vary over time or experiments.

where $\Delta S = S(\mathbf{m}_{new}) - S(\mathbf{m}_{old})$. The Root Mean Square (RMS) error used to quantify the data misfit is:

$$\mathrm{RMS}^2 = \frac{1}{n}\sum_{i=1}^{n}\left(\frac{g^i(\mathbf{m}) - d^i_{obs}}{d^i_{obs}}\right)^2 \tag{16}$$

where n denotes the number of measurements. The optimization is done with a Markov-Chain-Monte-Carlo (MCMC) sampler.

2.3. Alteration index

In this paper, we define a simple alteration index according to the presence of clays and zeolites on the surface conductivity (this works equally for the normalized chargeability). In that spirit, we divide the expression of the surface conductivity by its value for a fully altered volcanic rock that would corresponds to a smectite-rich clay cap. This yields

$$\mathfrak{I}_S(\%) = \frac{\frac{1}{F\phi}\mathrm{CEC}}{\left(\frac{1}{F\phi}\mathrm{CEC}\right)_{\mathrm{smectite}}} \approx \frac{300}{F\phi}\mathrm{CEC} \tag{17}$$

We can also write the alteration index for the kaolinite-rich domains associated with the upwelling of acidic fluids as,

$$\mathfrak{I}_K(\%) = 100\frac{\frac{1}{F\phi}\mathrm{CEC}}{\left(\frac{1}{F\phi}\mathrm{CEC}\right)_{\mathrm{kaolinite}}} \approx \frac{12}{F\phi}\mathrm{CEC} \tag{18}$$

The first index can be used to quantify the alteration in the areas dominated by near-neutral pore water from the ground surface down to the formation of the clay cap shown in Fig. 1 (Argillic zone, SEAL1). The second index can be used to quantify the formation of kaolinite associated with the upwelling of acidic ground waters close to the magmatic conduits in the phyllic zone (Fig. 1).

3. Laboratory investigations

Our goal in this paper is to characterize the electrical properties of stratovolcanoes like the one sketched in Fig. 1. We are especially

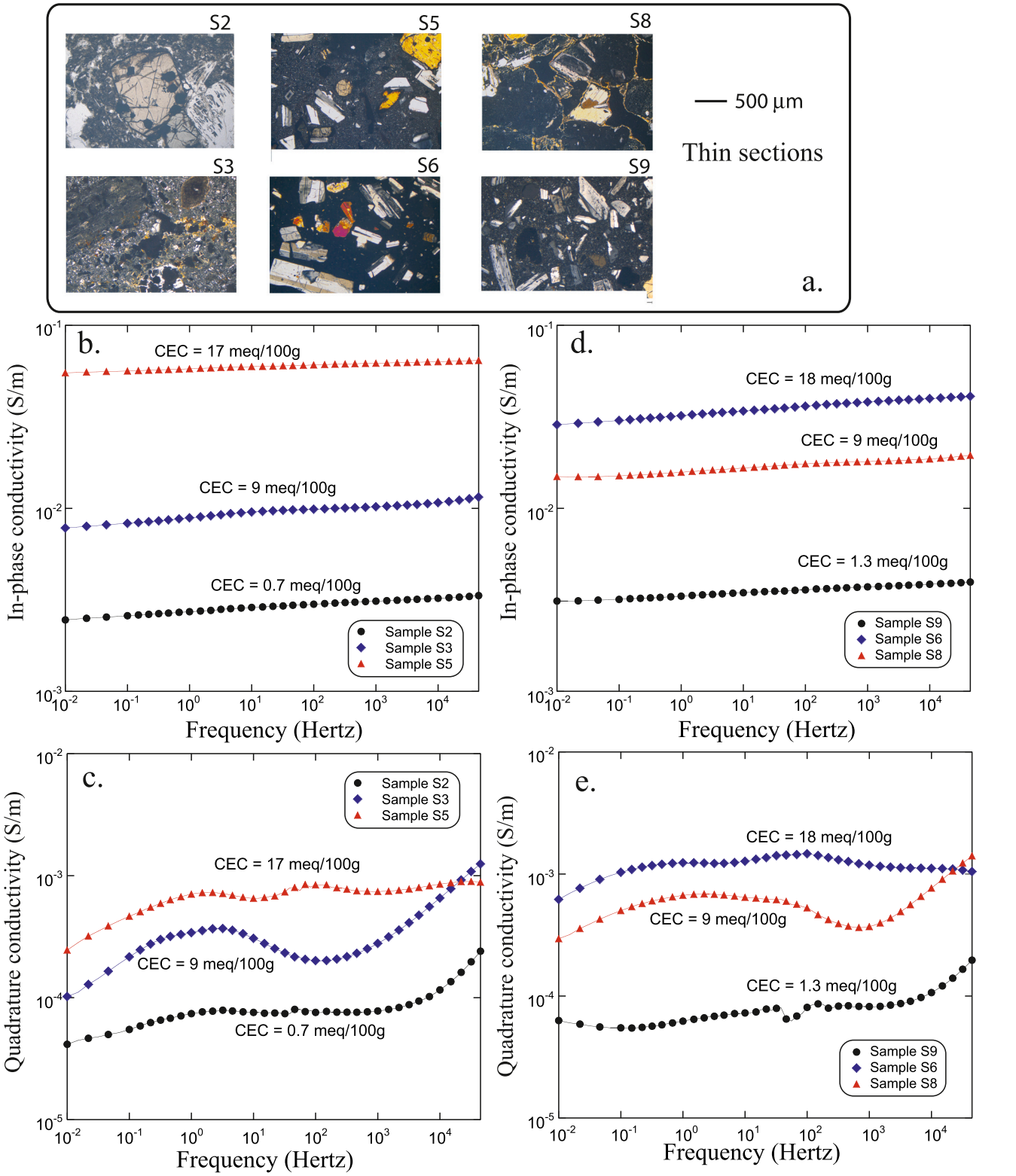

Fig. 4. Complex conductivity spectra of six selected core samples from La Soufrière stratovolcano characterized by three distinct values of their cation exchange capacity (pore water conductivity of 0.1 S m^{-1}, 25 °C). a. Thin sections. b. In-phase conductivity spectra of core samples S2, S3, and S5. c. Quadrature conductivity spectra of core samples S2, S3, and S5. d. In-phase conductivity spectra of core samples S6, S8, and S9. e. Quadrature conductivity spectra of core samples S6, S8, and S9.

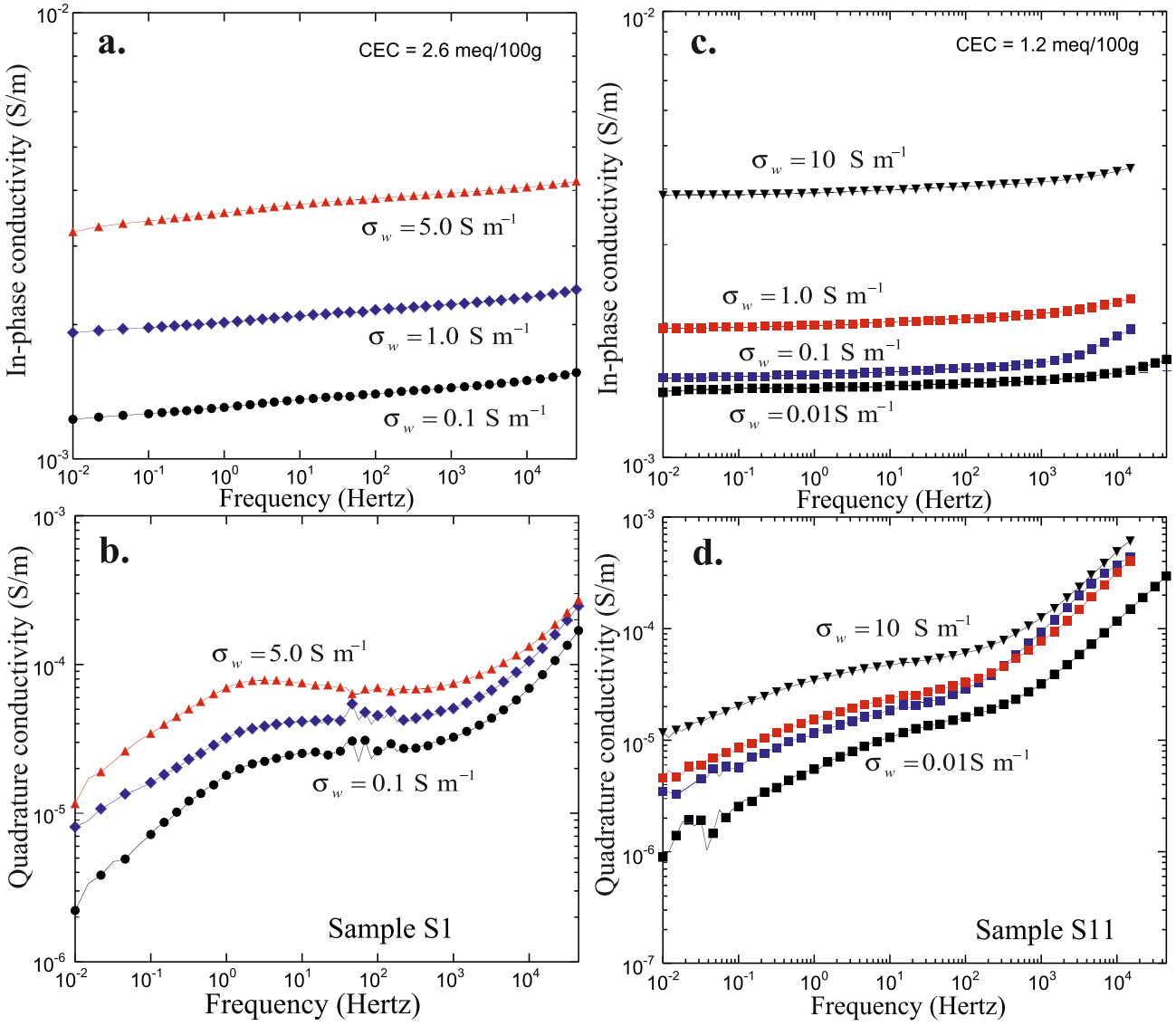

Fig. 5. Complex conductivity spectra. a. In-phase conductivity of sample S1 from La Soufrière stratovolcano at three salinities. b. Quadrature conductivity of sample S1 from La Soufrière stratovolcano at three salinities. c. In-phase conductivity of sample S11 from Papandayan stratovolcano at four salinities. d. Quadrature conductivity of sample S11 from Papandayan stratovolcano at four salinities. These spectra can be fitted with the double Cole Cole model described in Section 2.2.

interested in using induced polarization to image two types of altered areas (1) altered areas associated with the upwelling of hydrothermal fluids because they channel the acidic fluids responsible for the formation of kaolinite and (2) the formation of clay caps that are rich in smectite. The first step is to collect core samples in altered and non-altered areas in order to understand the connection between alteration and their induced polarization properties.

3.1. Core samples and experiments

We selected 10 core samples from La Soufrière volcano and 22 samples from the Baru crater of Papandayan (see position in Mazot et al., 2008, see Fig. 2). All these andesitic core samples were collected on outcrops based on their distinct porosity and alteration levels (Table 1). The samples for Papandayan are the same than those used in Ghorbani et al. (2018) but were measured at 6 salinities to further check the linear character of the dependence between the conductivity of the samples and the conductivity of the pore water.

Samples from la Soufrière are lavas and debris flow deposits (Table 1) from fresh states to samples exhibiting different degrees of alteration. The fresh lava samples (FL) are light to hard grey in colour, with phenocrysts of plagioclase, orthopyroxene, clinopyroxene and magnetite from 500 μm to 2 mm in size, their proportion ranges from 10 to 50%. The microlithic matrix is composed by the same phases. The glass phase fraction is very low. The porosity of this facies ranges from 0.11% with low density of unconnected cracks to 11.6% with a vesicular porosity. The slightly to moderate altered lava facies is a vesicular lava, phenocrysts similar to the fresh facies are slightly altered, cracks and vesicle are partly filled by secondary minerals Ti- Fe- Mn- oxydes, baryte, chlorite and muscovite. Fresh debris flow (FSF) are formed by centimetric to decametric clasts englobed in matrix of different compositions. In clasts the composition and the texture are similar to those of fresh lava material. The matrix is composed by the same primary mineral assemblage with clay and oxydes, their grains size could be largely lower (Navelot, 2018). Their porosity is high (env. 30%), alteration for the moderated and highly altered facies does not change the porosity values. For moderately altered facies, plagioclases are generally not affected, and pyroxenes are largely dissolved and replaced by clayey minerals, actinolite, pyrite and quartz. For highly altered facies initial phenocrysts, mesostase, and glass matrix are recrystallized to clay, iron

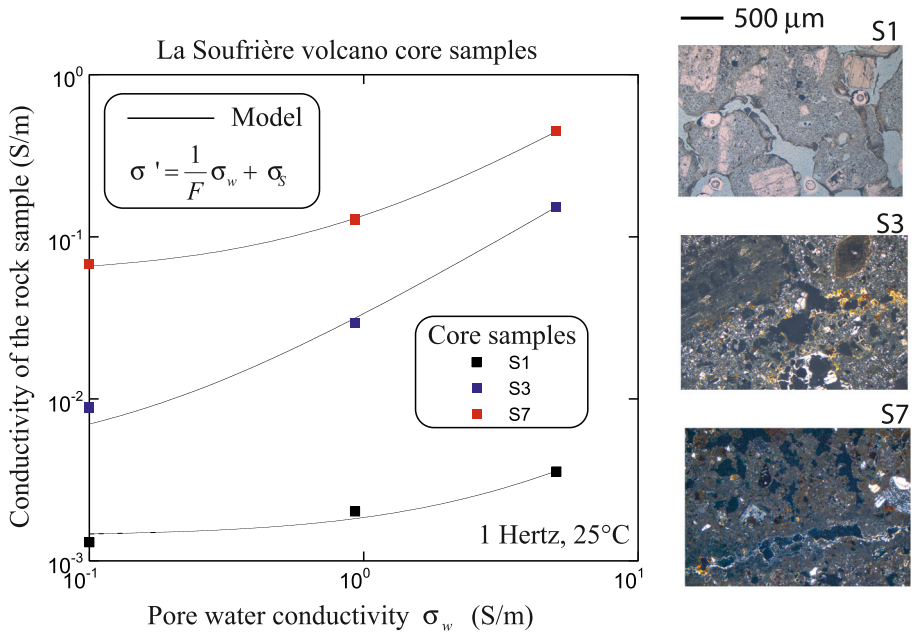

Fig. 6. In-phase conductivity (at 1 Hz) versus pore water conductivity for three core samples of La Soufrière volcano (the thin sections of the three core samples are shown). The trends are used to determine the surface conductivity σ_S and formation factor F for each core samples S1, S3, and S7.

Table 3
Electrical properties at 0.1 S m^{-1} (NaCl, 25 °C). Samples S1 to S10 belongs to la Soufrière while samples S11 to S32 belongs to Papandayan. The "partial" normalized chargeability is determined as M_n(1 Hz-1 kHz) = σ'(1 kHz) - σ'(1 Hz). The parameter F denotes the formation factor and σ_S denotes the surface conductivity (S m^{-1}) of the core samples.

Sample ID	σ' (S m^{-1}) (1 Hz-)	σ' (S m^{-1}) (1 kHz)	M_n (S m^{-1}) (1 Hz-1 kHz)	σ"(S m^{-1}) (32 Hz)	F (–)	σ_S (10^{-3} S m^{-1})
S1	0.001443	0.001305	0.00013844	2.61E-05	2500	0.0014
S2	0.003111	0.0027246	0.00038658	7.39E-05	133.3	0.0040
S3	0.010196	0.0088690	0.0013272	0.000232	33.9	0.0040
S4	0.050898	0.0440229	0.0068754	0.00147	17.6	0.0678
S5	0.062070	0.0578692	0.0042017	0.000737	75.8	0.0765
S6	0.038091	0.0320834	0.0060085	0.001416	25.1	0.0518
S7	0.027585	0.0262947	0.0012907	0.000197	13.0	0.0583
S8	0.018009	0.0157319	0.0022773	0.000615	46.9	0.0187
S9	0.003722	0.0033121	0.00040997	7.931E-05	63.3	0.00110
S10	0.032919	0.0283285	0.0045914	0.001479	44.1	0.0275
S11	0.001430	0.001490	6.000011e-05	1.3500e-05	4978	0.00175
S12	0.000684	0.0008900	0.00020600	4.7300e-05	8622	0.000836
S13	0.001840	0.002040	0.00019999	4.2400e-05	2557	0.00212
S14	0.001330	0.001960	0.00063000	0.00014300	2356	0.00195
S15	0.000780	0.0008400	5.999999e-05	1.3700e-05	1788	0.000803
S16	0.002000	0.002170	0.00016999	3.4600e-05	6262	0.00277
S17	0.001720	0.001840	0.00012000	2.9400e-05	1083	0.00217
S19	0.001230	0.001410	0.00018000	3.7300e-05	2523	0.00155
S20	0.002890	0.003400	0.00051000	0.00011900	1471	0.00360
S21	0.001320	0.001430	0.00010999	2.7000e-05	381.0	0.00115
S22	0.003200	0.003280	8.000014e-05	2.1200e-05	749.0	0.00400
S23	0.001840	0.001880	3.999996e-05	1.0200e-05	5235	0.00249
S24	0.0578	0.0591	0.0013	2.760e-04	5.38	0.00997
S25	0.0825	0.0859	0.0034	6.69e-4	4.01	0.03365
S26	0.0975	0.1010	0.0035	8.02e-4	4.89	0.031809
S27	0.0397	0.0404	0.0007	1.33e-04	5.74	0.00421
S28	0.457	0.465	0.008	4.93e-4	5.38	0.0328
S29	0.0371	0.0389	0.0018	3.75e-4	5.35	0.0393
S30	0.0893	0.0917	0.0024	4.46e-4	4.98	0.0253
S31	0.202	0.204	0.002	3.13e-5	3.79	0.0210
S32	0.0285	0.0292	0.007	1.32e-4	8.14	0.01005

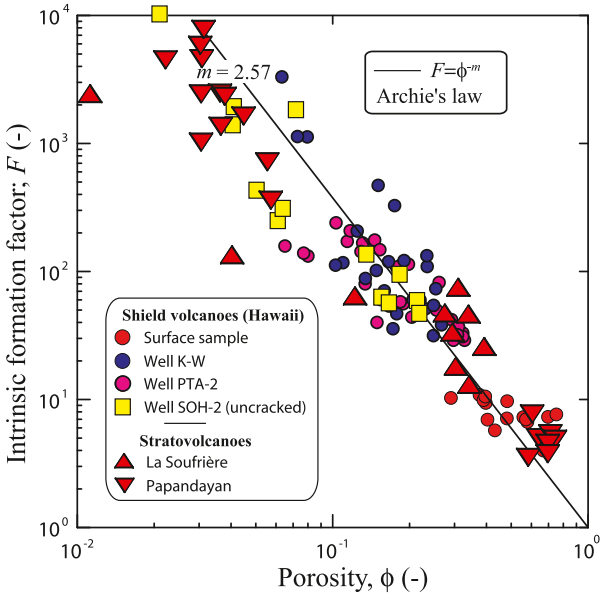

Fig. 7. Formation factor versus porosity for the volcanic rocks from the shield volcanoes of Hawaii and the 10 core samples from the La Soufrière stratovolcano and 22 samples from Papandayan stratovolcano. The data are fitted with an Archie's law representing a power law between the two parameters. The value of the porosity exponent is $m = 2.57 \pm 0.15$. Some low-porosity core samples exhibit some cracks with an exponent m comprised between 2.6 and 1.5. The Hawaii data are from the studies by Revil et al. (2021). We used 10 new core samples from La Soufrière volcano and 22 samples from the Baru crater of Papandayan (the same as used in Ghorbani et al., 2018).

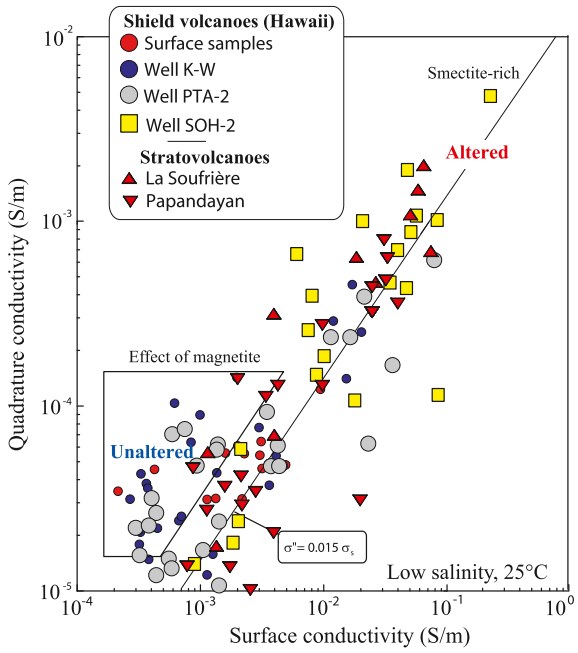

Fig. 8. Magnitude of the quadrature conductivity versus surface conductivity (at a pore-water conductivity of approximately 0.1 Sm^{-1} and taken at 1 Hz or 32 Hz) for volcanic rocks using literature data (shield volcanoes, filled circles, K—W stands for the Keller's well) and Well SOH-2 (yellow-filled squares), both in Hawaii. The so-called 'surface samples' have been collected in 2015 at the ground surface in the caldera of Kilauea around the Halema'uma'u crater. The linear trend is expected to be independent of the value of the formation factor, saturation, and temperature. Since surface conductivity is not affected by the presence of magnetite, it is a safer alteration indicator than the quadrature conductivity, which depends also on the presence of magnetite. There are 93 samples in total for shield volcanoes and 32 samples for the stratovolcanoes (red filled triangles). The Hawaii data are from the studies by Revil et al. (2021). We used 10 new core samples from La Soufrière volcano and 22 samples from the Baru crater of Papandayan (the same as used in Ghorbani et al., 2018). (For interpretation of the references to colour in this figure legend, the reader is referred to the web version of this article.)

oxide, calcite and quartz mineral (see Navelot et al., 2018, Navelot, 2018 and Table 2).

The samples from Papandayan are mainly basaltic andesites, pyroxene andesites, and pyroxene dacites (Asmoro et al., 1989). The Papandayan core samples contain pyroclasts with clinopyroxene crystals with simple core-rim zoning, euhedral magnetite crystals, unresorbed amphiboles, and iron oxides. Petrological studies on Papandayan lavas show that the most abundant alteration minerals in the altered materials are polymorphs of silica, pyrite, pyrophyllite, natroalunite, and kaolinite (Mazot, 2005; Mazot et al., 2008). It is important to remember that magnetite and pyrite are both semi-conductors that can play a strong role in induced polarization (Schlumberger, 1920; Revil et al., 2021).

The porosity of the core samples was determined from the dry and water-saturated weights of the core samples and their total volume measured by immersion. The CEC (Cation Exchange Capacity) measurements were performed with the cobalt hexamine method using 2 g of crushed rocks and a calibrated spectrophotometer at 472 nm (see the procedure in Aran et al., 2008) and Revil et al. (2017a, 2017b). CEC is an important parameter providing a proxy for the degree of alteration of these rocks especially regarding the amount of clay minerals (especially smectite), kaolinite, and zeolite (Revil et al., 2002). The porosity and CEC values of the core samples are reported in Table 1. The pH of the solutions was not buffered and is also reported in Table 1. It is generally close to the neutral value except for sample S7 for which the equilibrium pH is acidic at pH = 3.7. The specific surface area (in m^2/g) of the core samples was determined using the BET nitrogen adsorption technique (Brunauer et al., 1938, see Table 1). For the BET measurements, the core samples were first dried at 100 °C (N_2, 77 K, partial pressure P/P° comprised between 0.05 and 0.3).

Frequency-domain induced polarization measurements were performed over the frequency range 10 mHz-45 kHz using the ZELSIP04-V02 impedance meter (Zimmermann et al., 2008, 2019). For the unconsolidated core samples, we used the core holder described in Revil et al. (2017c). We measured the complex-valued impedance (amplitude and phase) that is converted to a complex conductivity with a geometrical factor depending on the position of the electrodes and boundary conditions for the electrical potential around the core surface external boundary (Jougnot et al., 2010).

For the consolidated core sample, the sample holder is shown in Fig. 3. Non-polarizable Ag/AgCl medical electrodes were used for both the current injection (electrodes A and B) and potential electrodes M and N. Typical complex conductivity spectra for low and high Cation Exchange Capacity (CEC) core samples are shown in Fig. 4. These core samples correspond to poorly and highly altered core samples, respectively. Therefore, Figs. 4 and 5 show how alteration affects both the in-phase and quadrature conductivity, respectively.

For the core samples from La Soufrière volcano, three saline solutions are used with the following pore water conductivities σ_w(NaCl, 25 °C) = 0.1, 1.0, and 5.0 S m^{-1}. Figs. 5a and b show the complex conductivity of sample S1 for these three salinities. For the core samples from Papandayan volcano, we used 6 salinities corresponding to the following pore water conductivities σ_w(NaCl, 25 °C) = 0.01, 0.1, 1.0, 5.0, 10.0, and 15 S m^{-1}. Figs. 5c and Fig. 5d show the complex conductivity at three salinities for sample S11 from Papandayan. The first saturation was always done under vacuum using washed and dried core samples and then the subsequent salinities were done by diffusion in a brine of higher salinity. The solution used to saturate the samples is degassed so it sucks any trace of air remaining in the pore space of the core samples (also degassed) during the infiltration of the water front. Each time we change

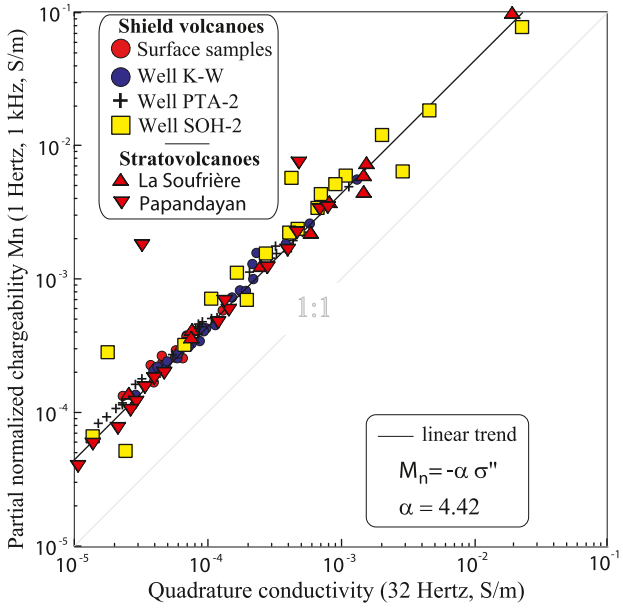

Fig. 9. Normalized chargeability (1 Hz-1 kHz) versus the quadrature conductivity for the volcanic samples from Hawai'i (low salinity, NaCl, 25 °C). The "partial" normalized chargeability is here determined as the difference in the in-phase conductivity between 1 Hz and 1 kHz while the quadrature conductivity is determined at the geometric mean frequency of 32 Hz. The plain line corresponds to a linear trend. The theory predicts that this trend is independent of the presence of magnetite (or pyrite) in the volcanic rocks. There are 93 samples in total for the shield volcanoes in Hawaii and 32 additional samples from La Soufrière and Papandayan. The value of the coefficient α can be predicted from the theory. The Hawaii data are from the studies by Revil et al. (2021). We used 10 new core samples from La Soufrière volcano and 22 samples from the Baru crater of Papandayan (the same as used in Ghorbani et al., 2018).

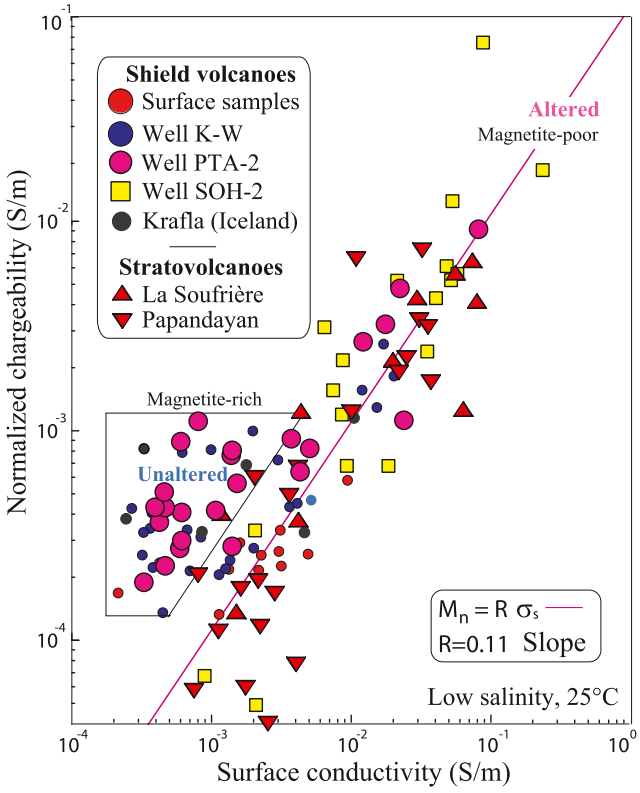

Fig. 10. Linear relationship between normalized chargeability (determined between 1 Hz and 1 kHz as the difference in the in-phase conductivity, low salinity, NaCl, 25 °C) and the surface conductivity for the volcanic samples). The measured slope leads to the following value of the dimensionless number $R = 0.11$. Note that most of the samples located in the unaltered box of the figure have been collected at the ground surface or cored in shallow formations. The Hawaii data are from the studies by Revil et al. (2021). We used 10 new core samples from La Soufrière volcano and 22 samples from the Baru crater of Papandayan (the same as used in Ghorbani et al., 2018). The data from Krafla are from Revil et al. (2019).

the salinity of the pore water by diffusion, we wait at least 1 month before measuring the conductivity of the core samples until a clear plateau is reached. In addition, we determine the characteristic diffusion time used to change the salinity of the pore water. We prefer diffusion-salinization rather than diffusion- desalinization in order to keep the diffusion process efficient at the core sample / water interface. That said, sometimes starting with low salinities may be a problem with smectite-rich core samples because of their very high swelling pressure that can disaggregate the texture of these samples during the swelling process at low salinities.

We observe that the magnitude of both the in-phase and quadrature conductivity of the core sample increases with the salinity of the pore water, which is consistent with models of the electrical double layer combined with speciation models for silicates (see for instance Revil and Skold, 2011; Niu et al., 2016).

3.2. Formation factor and Archie's law

We select the in-phase conductivity data at 1 Hz and plot them as a function of the pore water conductivity σ_w (see Fig. 6 for core samples S1, S3, and S7). As in Revil et al. (2017a, 2017b) and Revil et al. (2019), these data are fitted with Eq. (6), where the values of the (intrinsic) formation factor F and surface conductivity σ_S are reported in Table 3. A complete description of the procedure is explained in Revil et al. (2017a, 2017b) and Revil et al. (2021) and will not be reported here. Surface conductivity is associated with conduction in the electrical double layer coating the surface of the grains (van Olphen, 1957; van Olphen and Waxman, 1958; Bussian, 1983; Lyklema, 2002) and the inverse of the formation factor F appears as an effective porosity for the transport of electrical charges by electro-migration (Bernabé and Revil, 1995; Revil and Cathles, 1999). The formation factor is plotted versus the (connected) porosity in Fig. 7 in order to fit Eq. (8) respectively. With the exception of the two samples with the lowest porosities, the dataset conforms to the results obtained using the volcanic rocks from shield volcanoes i.e.,$F = \phi^{-m}$ with $m = 2.57 \pm 0.15$. Samples with cracks are generally charactterized by smaller cementation/porosity exponent m in the range 1.5–2.5.

3.3. Alteration, surface conductivity, and induced polarization

In Figs. 8 to 11, we check that the relationships obtained in Revil et al. (2021) for shield volcanoes are consistent with the new datasets for stratovolcanoes. In Fig. 8, we plotted the quadrature conductivity versus the surface conductivity. In a way consistent with the predictions of the dynamic Stern layer discussed in Revil et al. (2021, see also Weller et al., 2013), we see that quadrature conductivity and surface conductivity are linearly related to each other. The concept of dynamic Stern layer, first developed in the realm of colloidal chemistry (Zukoski and Saville, 1986a, 1986b), can be used to understand this type of trend.

Fig. 9 shows the correlation between the normalized chargeability and the quadrature conductivity. This relationship can be predicted using a broad distribution of relaxation times assumption corresponding to the so-called constant phase approximation (Revil et al., 2017c). Since the normalized chargeability and the quadrature conductivity are strongly related to each other and since the quadrature conductivity is related to the surface conductivity, it is not surprising to observe that the

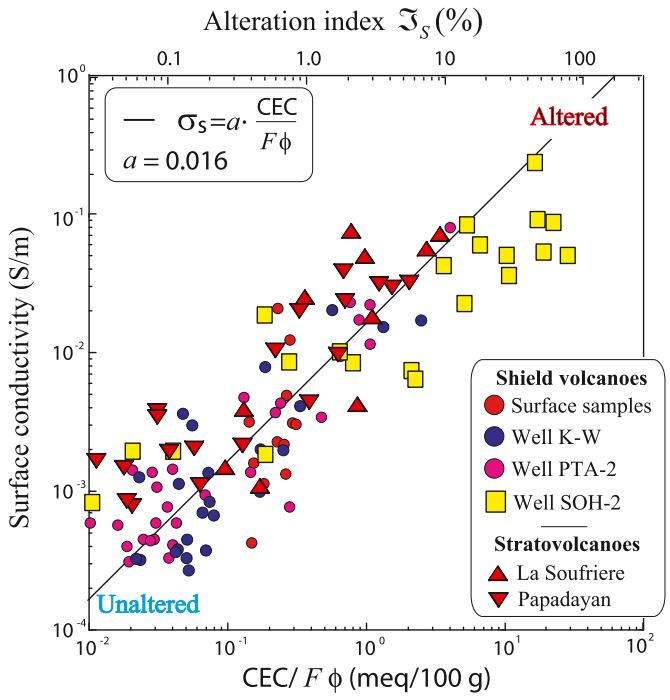

Fig. 11. The surface conductivity (S m^{-1}) versus the reduced (or normalized) CEC defined as CEC/$F\phi$ where CEC denotes the cation exchange capacity (expressed here in meq/100 g), F the formation factor, and ϕ the connected porosity (1 meq /(100 g) = 963.2C kg^{-1}). There are 93 samples in total. This trend is independent of the presence of metallic conductors in the mixture. According to our model, the slope is equal to $B\,\rho_g$. Keeping in mind that the CEC is here expressed in meq/100 g, using $B(Na^+, 25\ °C) = 3.1 \times 10^{-9}$ $m^2 s^{-1}$ V^{-1} (effective mobility of the counterions in the electrical double layer) and ρ_g = 2900 kg m^{-3} (grain density) we have $a = 0.009$ close to the observed trend $a = 0.016 \pm 0.08$.

normalized chargeability and the surface conductivity are linearly-related (Fig. 10, see also Weller et al., 2013).

Finally, Fig. 11 shows that the normalized chargeability (hence the quadrature conductivity and the surface conductivity) can be related to the cation exchange capacity divided by the bulk tortuosity of the pore space defined as the product of the formation factor by the (connected) porosity. In other words, the dynamic Stern layer model and the constant phase approximation offer complementary pictures to analyze surface conductivity and induced polarization properties of volcanic rocks using a physics-based set of relationships between the key-material properties. This approach is simple and effective without the need of flush factors as done in the literature. It does not matter if the rocks are from stratovolcanoes or shield volcanoes, the trends are universal. This is one of the main results obtained in this paper. In Fig. 11, we also the smectite-based alteration index defined by eq. (17). This indicates how the degree of alteration associated with the formation of clays affects the electrical properties investigated in this paper.

3.4. Alteration path

Fig. 12 displays the geoelectrical alteration path observed for volcanic rocks from shield volcanoes like in Hawaii. This path is obtained by plotting the quadrature conductivity (e.g., at 1 Hz) versus the CEC of the rock used as a proxy of alteration. First the magnetite responsible for a strong polarization of the rock disappears because of the increase of temperature. Geothermal areas exhibit a destruction of magnetic minerals by hydrothermal activity through both low-temperature oxidation (<350 °C, maghemitization) and fluid–rock interactions (e.g., Oliva-Urcia et al., 2011; Fujii et al., 2018). This leads to a decrease of the magnitude of the quadrature conductivity. Then the formation of

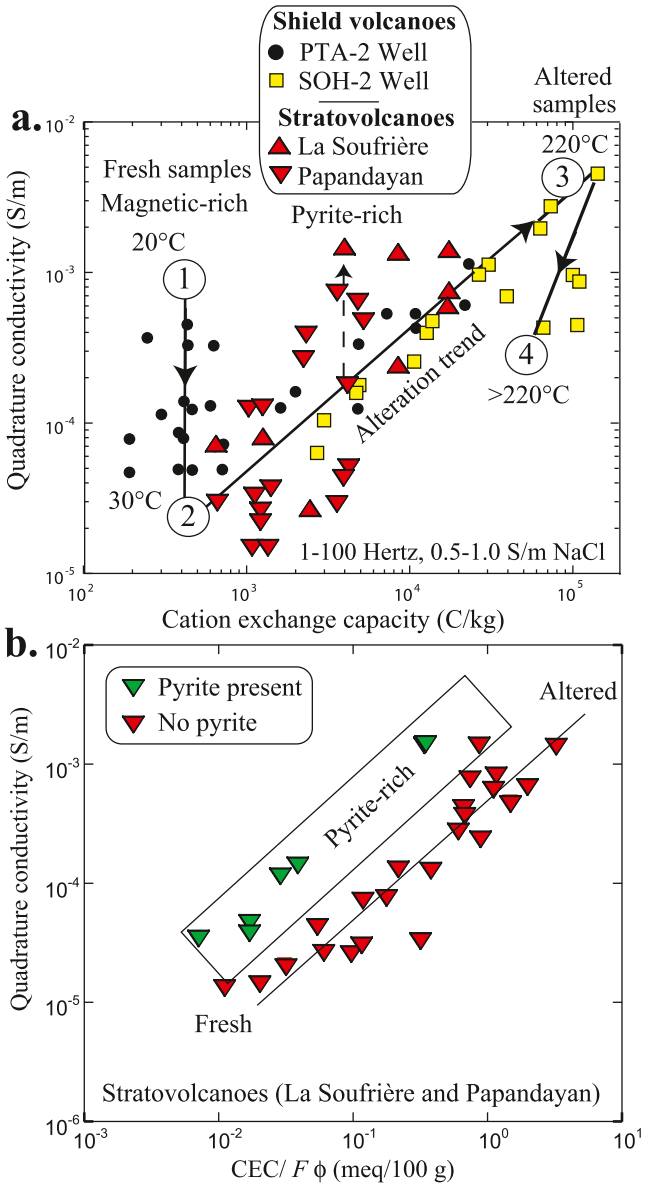

Fig. 12. Geoelectrical alteration path for the core samples. a. Quadrature conductivity versus CEC. trends from stage (1) corresponding to fresh magnetite-rich samples to stage (3) corresponding to smectite-rich strongly altered core samples. From stages (1) to (2) we observe the decrease of the magnetite content with the increase of the temperature with the depth of burial. The disappearance of magnetite results in rocks losing progressively their magnetic susceptibility. In stage (2), magnetite has disappeared and the alteration starts with an increase of the content in smectite until a temperature of 220 °C is reached at stage (3). Both porosity and CEC change along this trend. Above 220 °C, smectite is progressively replaced by chlorite and mixed-layer clays with a lower CEC. Porosity is probably not affected by these changes. b. Quadrature conductivity versus the normalized CEC (CEC divided by the bulk tortuosity). The pyrite-rich samples are from Papandayan volcano. The presence of pyrite is assessed by XRD analysis (see Table 2 and Navelot et al., 2019).

smectite as a result of alteration, increases progressively the CEC and the quadrature conductivity of the material. This occurs up to a temperature of 220 °C for which smectite is not stable anymore and outside of the areas associated with the upwelling of the acidic ground waters (Kristmannsdóttir, 1979; Flóvenz, 2005). Adding the data from the stratovolcanoes shows a similar geoelectrical alteration path. The higher dispersion in the data is partly explained by the fact that the samples we used have a high variation in their porosities. Still, they agree with the

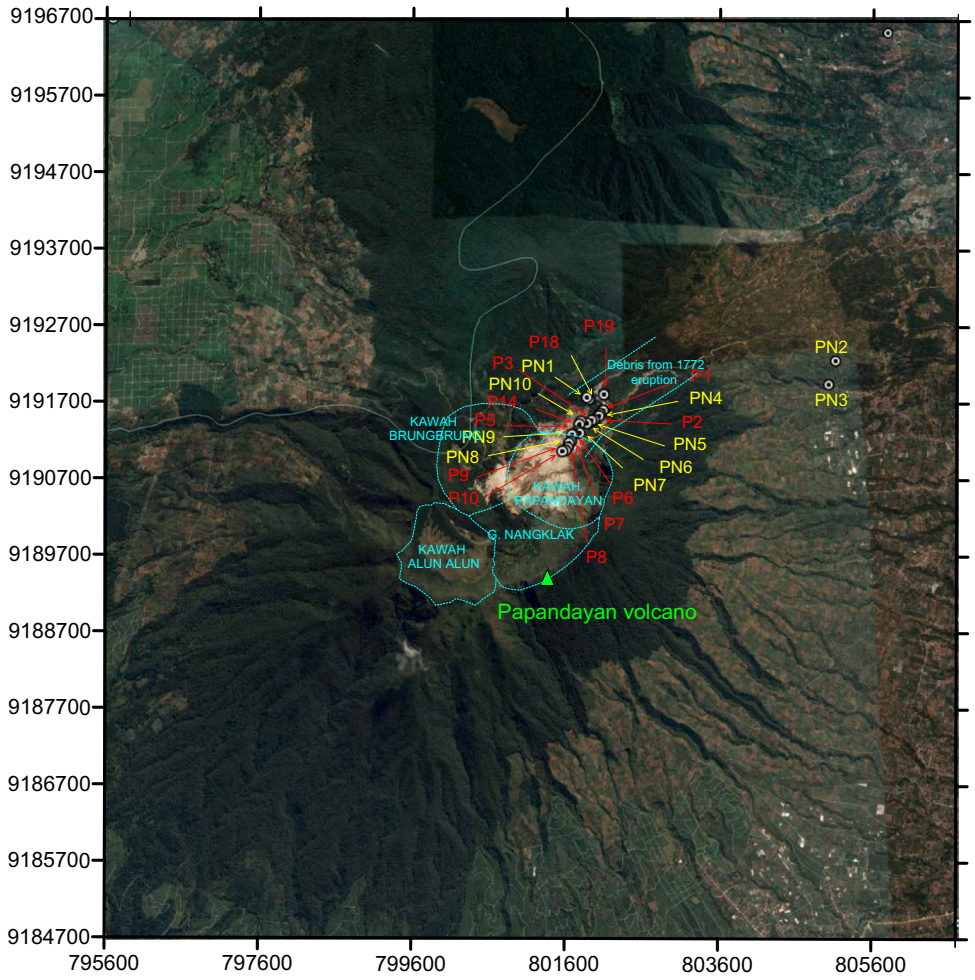

Fig. 13. Map of Papandayan volcano with the position of the core samples (from Ghorbani et al., 2018, Pi and PNi correspond to the consolidated and non-consolidated samples collected at outcrops). Coordinates: Easting – UTM (m) WGS84, Northing – UTM (m) WGS84. The core samples are the same as used by Ghorbani et al. (2018).

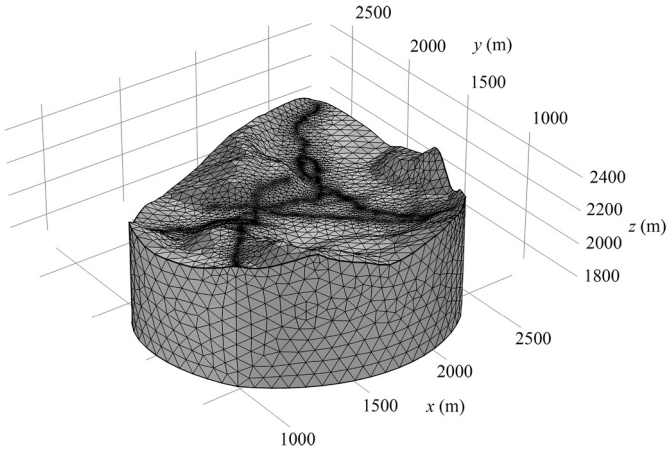

Fig. 14. Mesh used for the finite element computation of the forward problem and the inversion of the geophysical data. The high density of meshed on the ground surface underlines the position of the induced polarization surveys, which comprises 240 electrodes and 1800 apparent resistivity and chargeability data. The spacing between the electrodes is 30 m. The core domain comprises a total of 75,628 elements. The position of the profiles corresponds to the dark areas for which the mesh is strongly refined around the position of the electrodes.

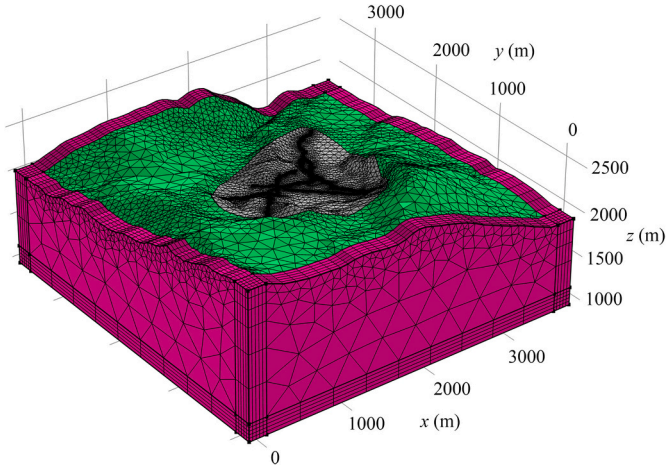

Fig. 15. Mesh of the whole domain used for the inversion of the field data. The core, the buffer and the boundary domains are in grey, green and red colors, respectively. A total of 113,752 elements are used for the whole domain to perform the finite element computations. (For interpretation of the references to colour in this figure legend, the reader is referred to the web version of this article.)

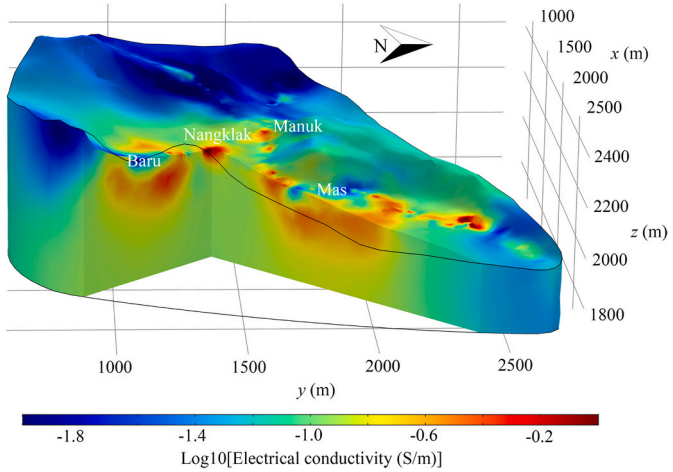

Fig. 16. 3D electrical conductivity tomogram of Papandayan volcano. The conductivity in some areas is close to 1 S m^{-1} like for the Soufrière volcano. These high conductivity subvolumes can be associated with the high salinity of the acidic pore fluids or with a degree of alteration.

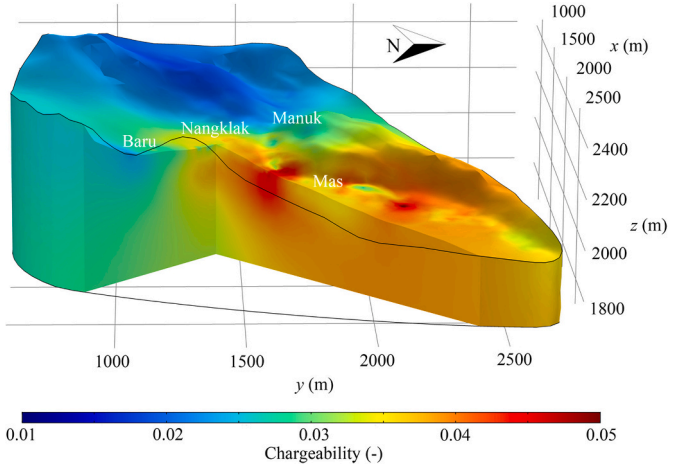

Fig. 17. 3D chargeability tomography of Papandayan volcano. The highest chargeability is close to 0.05 (50 mV/V).

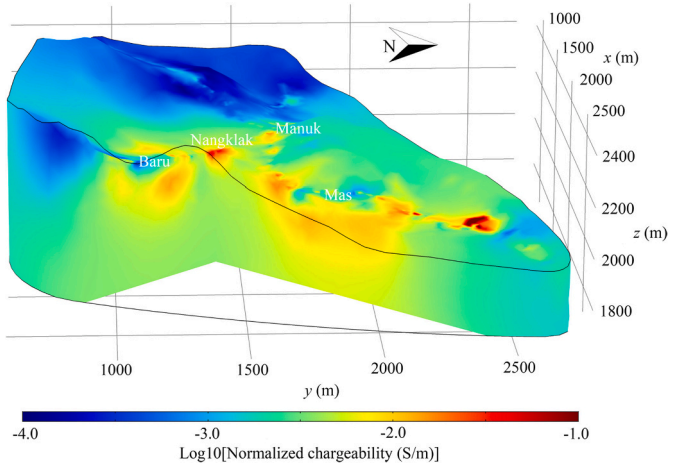

Fig. 18. 3D normalized chargeability tomogram of Papandayan volcano. The highest normalized chargeability is close to 0.10 S m^{-1} indicating a high level of alteration associated with the upwelling of high-temperature acidic pore fluids.

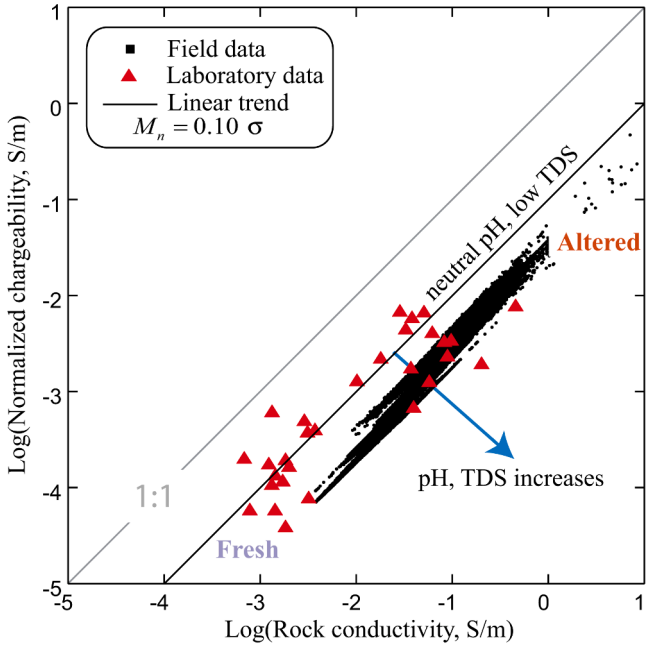

Fig. 19. Normalized chargeability versus conductivity of the volcanic rocks. The plain line (linear trend with $M_n = 0.10\ \sigma$) corresponds to the case for which surface conductivity dominates the conductivity response of the rocks with low salinity and near-neutral pore waters. In this condition, the normalized chargeability M_n is given by $M_n = R\ \sigma$ with $R \cong M_n / \sigma_S = 0.10$ and σ denotes the conductivity of the rock. The field data are consistent with a higher salinity / lower pH pore waters for which $M = M_n / \sigma < R$.

data obtained from shield volcanoes. Formation of pyrite occurs under reducing and acidic conditions (e.g., Oliva-Urcia et al., 2011). The presence of pyrite can however make the alteration path more complex since pyrite (like magnetite) has a strong polarization property as a semiconductor (see Ghorbani et al., 2018, for volcanic rocks). In Fig. 12, the presence of pyrite in some core samples was qualitatively assesses by XRD (X-Ray Diffraction) analysis (see Table 2).

4. Field application

4.1. The Papadanyan Stratovolcano

Papandayan volcano (Indonesia) belongs to the Sunda magmatic arc, which formed as a consequence of the northward subduction of the Indo-Australian plate beneath the Eurasian plate (Syahbana et al., 2014). It is located on the island of Java (7°323 S and 107°73′E) rising to an altitude of 2665 m above sea level (masl), 175 km away from Jakarta. Papandayan is a complex stratovolcano with several craters, the youngest of which breached to the northeast by the collapse during the catastrophic eruption in 1772 (Abidin et al., 2003, see Fig. 13). The 1772 summit crater consists of four main craters, Kawah Mas, Kawah Manuk, Kawah Nangklak, and Kawah Baru ("Kawah" means "Crater" in Indonesian, Syahbana et al., 2014). In the present study, we are interested in the 1772 summit crater because of its strong hydrothermal activity with fumaroles, sulfur-mud pools, hot springs, which forms as a typical example to characterize and monitor the hydrothermal system and the concomitant alteration of stratovolcanoes like La Soufrière volcanoes. Papandayan emits sulfur dioxide (SO_2, 4 t/day, Bani et al., 2013), hydrogen chloride (HCl), and carbon dioxide (CO_2). Like at La Soufrière volcano, the upwelling fluids containing acid gases across the hydrothermal zone beneath the crater produce acidic pore waters (Mazot et al., 2008; Bani et al., 2013). The mechanical weakness of the altered rocks is responsible for flank collapses.

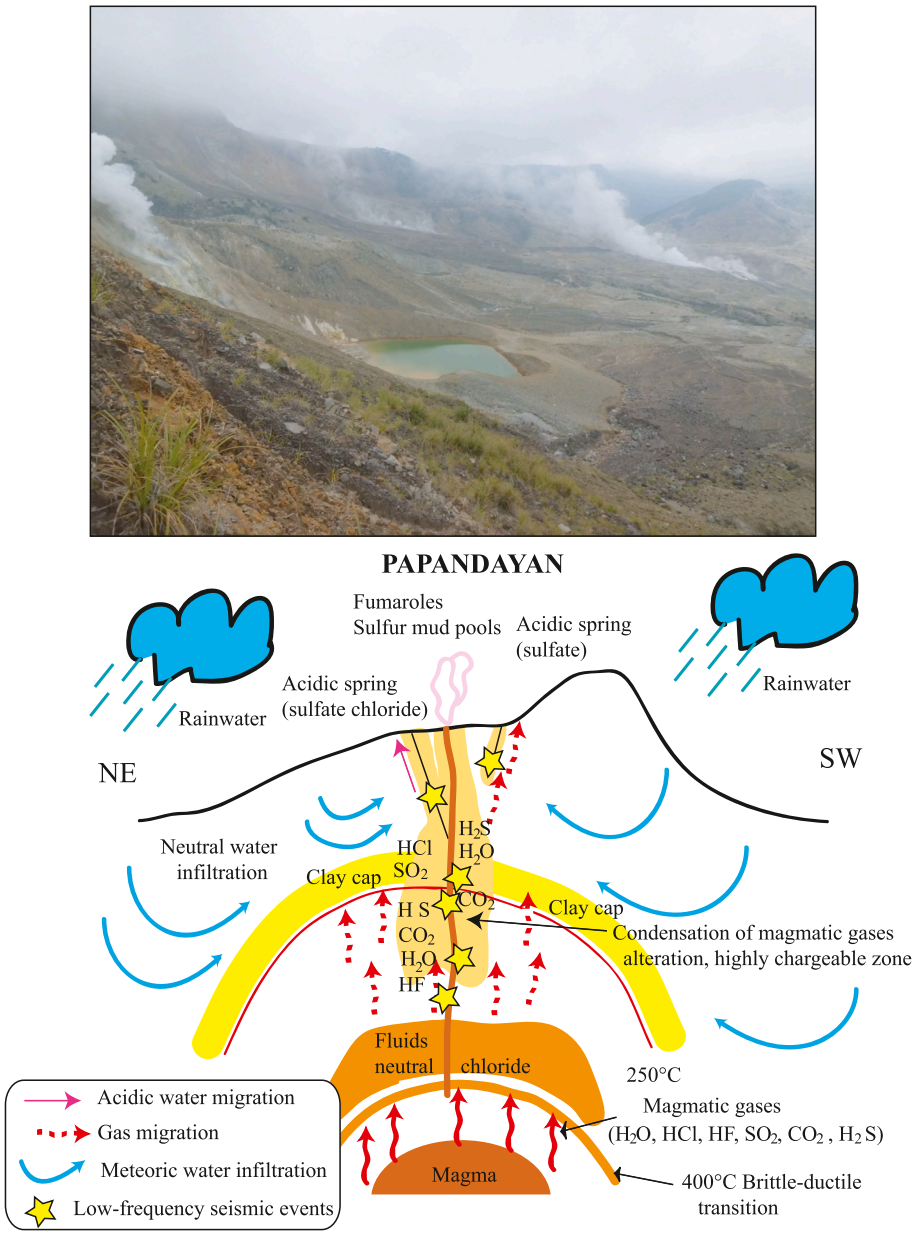

Fig. 20. Sketch of the altered zones associated with Papandayan volcano (modified from Mazot et al., 2008) showing the areas impacted by the alteration. Induced polarization is used to image these altered areas. The stars correspond to the low-frequency seismic events. The clay cap is rich in smectite while the altered area around the acidic conduits is rich in kaolinite.

4.2. Field investigations

A total of five resistivity / induced polarization profiles were acquired in the 1772 crater. Despite the strong topography of the site, this survey provides a reasonable way to cover this crater. Each profile is characterized by 48 electrodes (Fig. 14). The spacing between the electrodes is 30 m. All the profiles are measured by a Czech ARES II instrument with a Wenner-alpha array. The survey includes 240 electrodes and 1800 apparent resistivity and chargeability data were acquired. The first window of the ARES II instrument begins at 5 ms after the shutdown of the primary current. Each window has a duration of 100 ms. The present study focused on the second-window for the apparent chargeability, which is mostly free of the electromagnetic coupling effects.

Considering the strong topography of Papandayan volcano, we use the DLR SRTM high-resolution Digital Elevation Map (DEM) file to build the surface of our geometric model (see Figs. 14 and 15). We divide the whole model into three domains: the core, the buffer and the boundary domains, which as shown in grey, green and red colors in Fig. 15, respectively. Finite element method is used as a forward modeling tool (see Kemna, 2000). Since wireframes of connected triangles are more accurate and efficient than the conventional rectilinear grid for real-world scenarios (Qi et al., 2019), unstructured free tetrahedral meshes are used to discretize the geometric domain as shown in Figs. 14 and 15. To precisely capture the signal characteristics, meshes near the source and sink electrodes are locally refined in the core domain. Besides the meshing technique, the truncation of the simulation domain is another factor to influence the modeling accuracy. If the conventional Dirichlet boundary condition (the potential goes to zero at infinity, i.e., far away from the electrodes) is used, the simulation domain shall be sufficiently

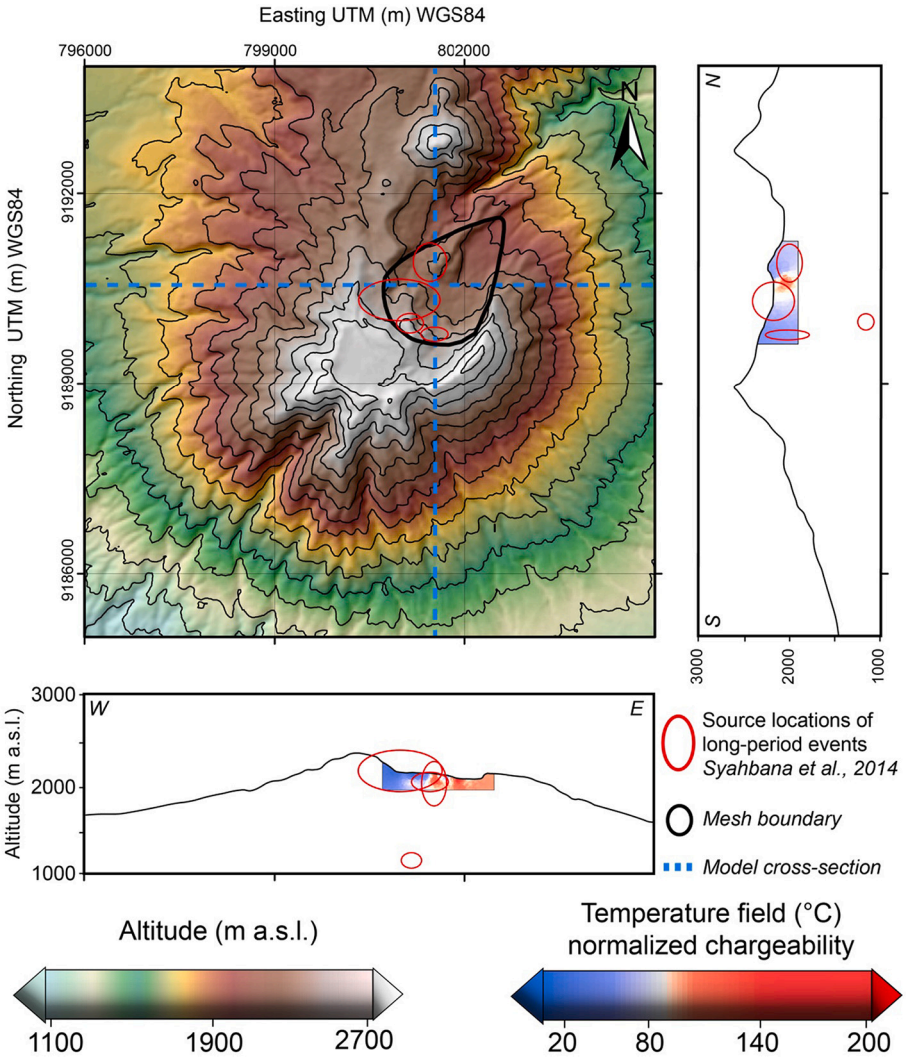

Fig. 21. Comparison between the long-period source locations (red circles) from Syahbana et al. (2014) and the temperature field (°C) along W-E and N-S cross sections (blue dotted lines). The solid black line indicates the central mesh domain used for the inversion of the induced polarization data. Long-period events are located in the central part of the volcano, matching the high temperature region inferred in this study. (For interpretation of the references to colour in this figure legend, the reader is referred to the web version of this article.)

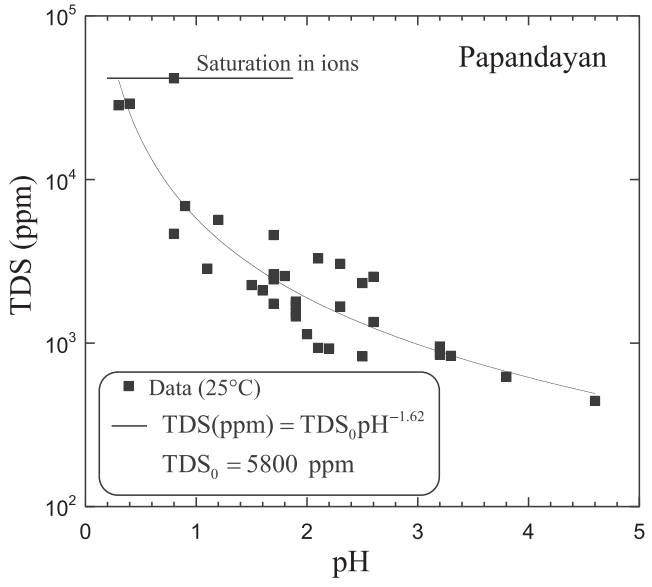

Fig. 22. Relationship between TDS (Total Dissolved content) and pH of the ground water ($r^2 = 0.55$). The data from Papandayan are used to fit a power law relationship between the two parameters (data from Mazot et al., 2008).

large that the outer boundary conditions will not affect the solution. Here we resort to the infinite element method to greatly reduce the domain size without losing accuracy (see Qi et al., 2019 for details). Finally 113,752 elements are generated for the whole domain and 75,628 for the core domain (Figs. 14 and 15).

Following Oldenburg and Li (1994), the time-domain induced polarization data inversions are performed in two steps: first we invert the conductivity (Fig. 16) and then the chargeability (Fig. 17). Since both conductivity and chargeability inversions are mathematically ill-posed, we use the regularized least-squares method by minimizing the objective function discussed in Qi et al. (2018) and Revil et al. (2021). The same procedure was used in the present paper. The Jacobian matrix is calculated by the adjoint method. Since Jacobian matrix calculations in each iteration are time-consuming, quasi-Newton using Broyden's method rather than Gauss-Newton is used (Broyden, 1965). The algorithm was benchmarked on synthetic and field data (see Qi et al., 2018) and will not be repeated here. When the inversion is completed, the normalized chargeability tomogram can be readily obtained by multiplying the conductivities and chargeabilities cell by cell (see Revil et al., 2021).

4.3. Results

The conductivity, chargeability and normalized chargeability tomograms are shown in Figs. 16–18, respectively. Compared with the

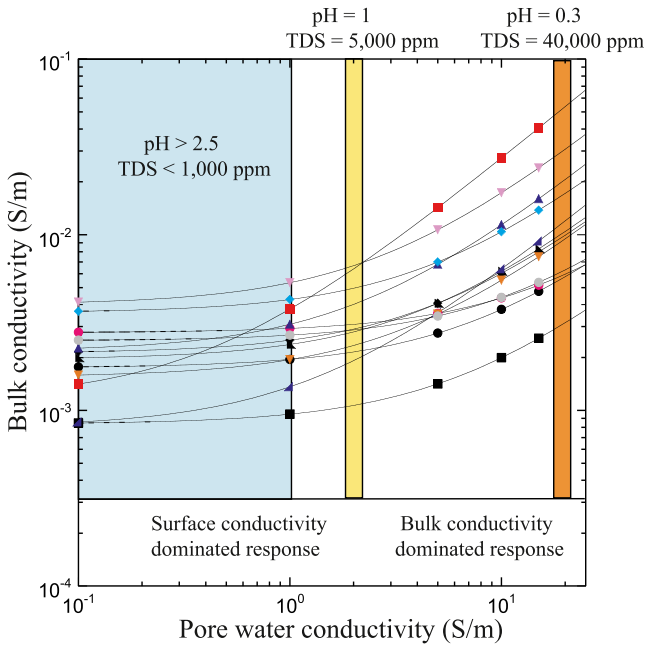

Fig. 23. Electrical conductivity of the consolidated core samples from Papandayan (samples S11 to S23) versus the pore water conductivity. The colored filled areas correspond to various conditions in terms of acidity and concomitant TDS. For pH ≥ 1, we can consider that surface conductivity plays a major role in the overall conductivity response of the volcanic rocks.

volume-cutting plot of these three parameters, the conductivity and normalized chargeability show similar pattern in the four craters (Mas, Manuk, Nangklak, and Baru). The normalized chargeability tomogram provides a way to image the alteration level below the craters. Electrical conductivity depends both on the pore water conductivity and alteration. In stratovolcanoes, the conductivity of the pore water can be very high in altered areas because of its acidity and ability to dissolve minerals. Therefore it is difficult to say, which contribution (bulk versus surface conductivity) would dominate the conductivity response. A plot of the normalized chargeability with respect to the conductivity is shown in Fig. 19. We can see that this ratio is around 0.03. The constant ratio R between the normalized chargeability and the surface conductivity is around $R = 0.10 \pm 0.02$ for volcanic rocks (Ghorbani et al., 2018; Revil et al., 2018). We can conclude that bulk conductivity plays an important role in controlling the conductivity of the volcanic rocks in the summit crater of Papandayan because of the high pore water conductivity associated with the upwelling of acidic highly saline brines, especially in high-porosity core samples.

The Mas crater is the most active vent in the summit of Papandayan (Triastuty et al., 2006; Mazot et al., 2008; Hasan et al., 2016). Besides, when comparing the normalized chargeability at the surface with the epicenters from the previous low-frequency seismic measurements as shown in Hasan et al. (2016), we found that they all coincide perfectly well with each other. This validates that vents of acidic ground water upflows are both responsible for low-frequency seismic events (Triastuty et al., 2006; Ohminato, 2006; Matoza and Chouet, 2010; Hasan et al., 2016) and high alteration levels as observed in the present paper and in Gresse et al. (2021). Indeed, low-seismic events are generally associated with resonance effects associated with the movement of fluids (magma,

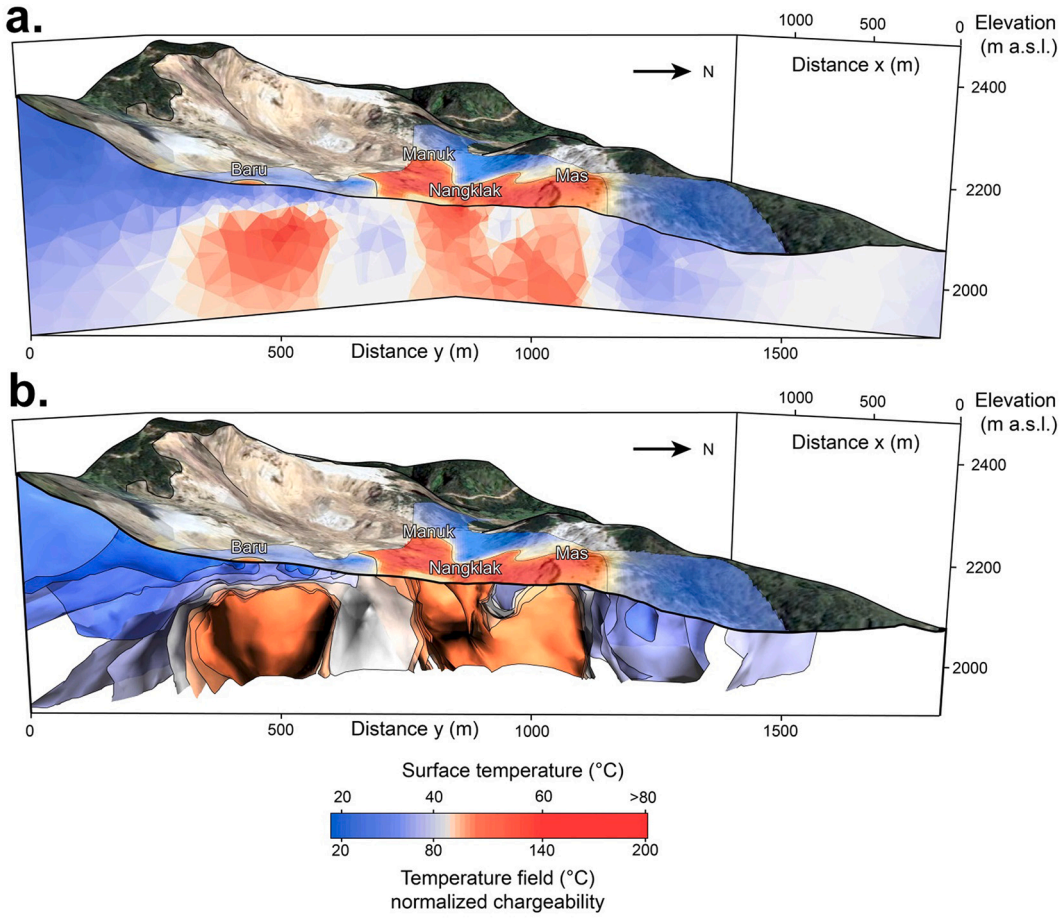

Fig. 24. Tomography of the temperature field using the normalized chargeability determined from the induced polarization measurements and comparison with the surface temperature field (from Byrdina et al., 2018). The normalized chargeability can be used to assess the position of the altered sub-volumes associated with the upwelling of the acidic hydrothermal fluids ("masl" stands for meters above sea level) and the formation of kaolinite. a. Side view of the temperature distribution. b. Isotherms.

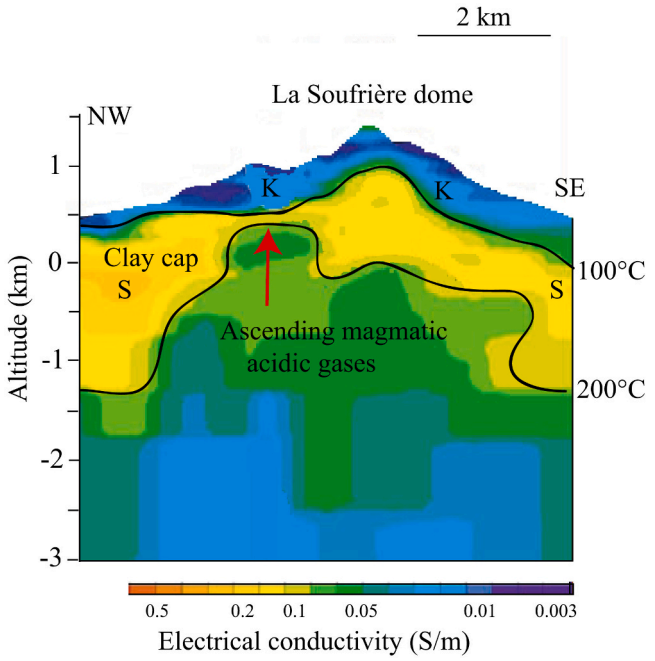

Fig. 25. Interpretation of the electrical conductivity tomogram of La Soufrière volcano showing the conductive clay cap (likely smectite –rich). The conductivity tomogram is from Raguenel et al. (2019). An induced polarization survey could confirm the importance of surface conductivity in explaining the conductivity variations at this stratovolcano and obtaining the porosity and CEC tomograms. K and S refer to kaolinite and smectite, respectively.

gas, water) in conduits (Kedar et al., 2021). Fig. 20 provides a sketch of such a mechanism and Fig. 21 show that the shallow long period seismic events (data from Syahbana et al., 2014) are consistent with this viewpoint.

5. Discussion

There are five points that we want to discuss here. The first is the role of surface conductivity in the overall conductivity response of strato-volcanoes. Fig. 19 plots the normalized chargeability versus the conductivity of the rock. In strato-volcanoes, the pore water pH and the TDS (Total Dissolved Salt, hence the pore water conductivity at a reference temperature of 25 °C) are correlated to each other (Fig. 22). We know that at low salinity, the conductivity response of the rock samples from Papandayan is dominated by the surface conductivity (Fig. 23). In this case, at neutral pH and a pore water conductivity of 0.1 S m^{-1} (25 °C, pH ~7), the normalized chargeability is just proportional to the conductivity of the rock with a slope of $R = 0.10$ (Revil et al., 2021 for shield volcanoes). It should be remembered that R is the ratio between the normalized chargeability and the surface conductivity. This prediction is consistent with the laboratory data (Fig. 22). The field data plot on a separate linear trend indicated that Papandayan stratovolcano is marked by acidic and high salinity ground waters for the central portion investigated in this paper. Still, as reported in Fig. 19, we see that surface conductivity cannot be neglected excepted by extremely acidic pore waters with a pH smaller than 1. This contrasts with the erroneous assumption (i.e., bulk conductivity dominates necessarily the surface conductivity) made by both Rosas-Carbajal et al. (2016) for La Soufrière volcano and Byrdina et al. (2018) for Papandayan volcano.

We also check the validity of the power-law relationship between TDS (Total Dissolved content) and pH of the ground water shown in Fig. 22 to other strato-volcanoes. For another stratovolcano, Mount Ciremai, Kuningan Regency, West Java, Indonesia, Dianardi et al. (2018) reported a TDS in the range 50 to 151 mg/L (1 ppm = 1 mg/L) for a pH range from 6.4 to 7.7 For pH = 7, the relationship provided in Fig. 22 yields a TDS of 240 mg/L, so close enough from the observed TDS range. However, some datasets do not conform to this trend (see for instance Joseph et al., 2013). We let this point for further investigations.

The second point we want to discuss is how to use the normalized chargeability tomogram to image the temperature field inside a strato-volcano. Temperature is one of the most important parameter to describe geothermal field (e.g., Békési et al., 2020). We have seen in this paper that the electrical properties of the volcanic rocks from strato-volcanoes are not that different from the electrical properties of the volcanic rocks from shield volcanoes. We can therefore use the temperature trend derived in Revil et al. (2021) to image the temperature field inside Papandayan. This is done in Fig. 24 using the following

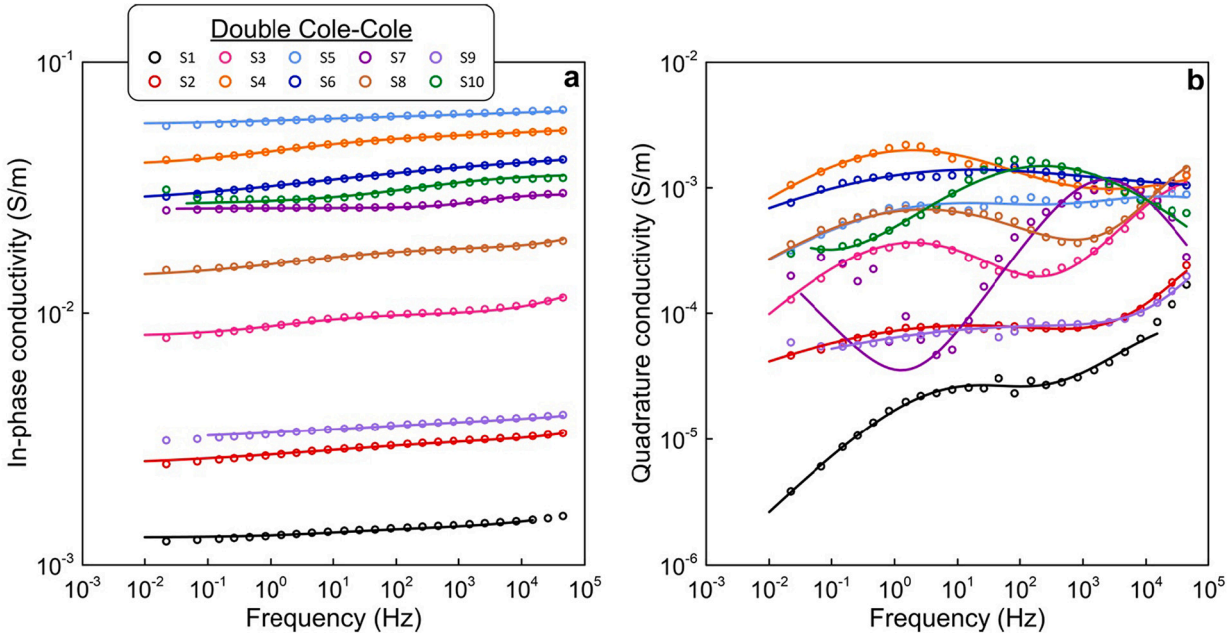

Fig. 26. Double Cole Cole fit of the complex conductivity spectra of the core samples from La Soufrière stratovolcano at the lowest salinity. a. In-phase conductivity spectra. b. Quadrature conductivity spectra. The Cole Cole parameters are reported in Table 4. The fit is done using the approach described in Section 2.2.

Table 4
Cole Cole parameters for the core samples from La Soufrière volcano. We use a Double Cole Cole parametrization of the complex conductivity spectra and a stochastic (Bayesian) inversion procedure. The subscript 1 refers to the low frequency (LF) polarization while subscript 2 refers to the high frequency (HF) polarization.

Sample ID	Sample ID	σ_∞ (S m^{-1})	M_1 (−) LF	M_2 (−) HF	c_1 (−) LF	c_2 (−) HF	τ_1 (s) LF	τ_2 (s) HF	RMS (%)
1	152–15	0.0018119	0.063732	0.22685	0.48	0.49	0.014	1.7e-06	0.41
2	165–15	0.0042758	0.20003	0.22812	0.23	0.72	0.012	5.7e-07	0.21
3	GD15.03	0.014034	0.13542	0.28887	0.47	0.64	0.087	2.2e-06	0.33
4	GD16.24	0.062867	0.19653	0.19443	0.38	0.28	0.099	6.9e-08	0.30
5	GD16.09	0.066070	0.075253	0.071987	0.33	0.38	0.034	4.0e-06	0.38
6	GD16.26	0.048111	0.24341	0.19221	0.25	0.20	0.024	1.0e-07	0.30
7	GD15.10	0.029914	0.095051	0.12314	0.55	0.72	592	6.9e-05	2.3
8	GD15.15	0.023497	0.20187	0.21185	0.35	0.74	0.055	1.3e-06	0.27
9	GD15.160	0.0049416	0.22396	0.16187	0.18	0.80	0.0011	4.3e-07	0.32
10	GD15.150	0.036049	0.046544	0.23934	0.58	0.42	62	0.00065	0.53

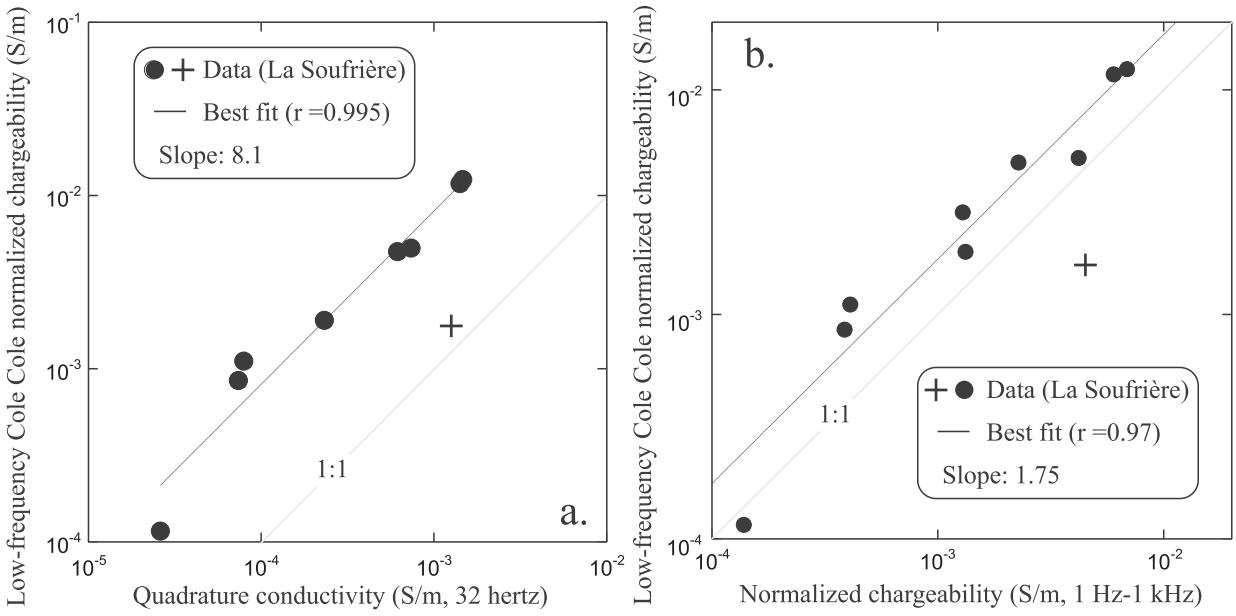

Fig. 27. Comparison between the Cole Cole normalized chargeability and either the partial normalized chargeability or the quadrature conductivity. a. Low-frequency Cole-Cole normalized chargeability (from Table 4) versus the quadrature conductivity at 32 Hz (see Table 3) for the samples from La Soufrière stratovolcano. The cross is the sample not used in the linear fit of the data. b. Low-frequency Cole-Cole normalized chargeability (from Table 3) versus the partial normalized chargeability determined as the difference of the in-phase conductivity between 1 Hz and 1 kHz (see Table 3) for the samples from La Soufrière stratovolcano. The cross denotes the result of a core sample not used in the linear fit of the dataset. In both cases, the slopes are those predicted by the model discussed in Revil et al. (2017c).

relationship $M_n(T) = M_0 T^{2.5}$ with $M_0 = 5.8 \times 10^{-8}$ (see Revil et al., 2021). A comparison is made with the surface temperature field of this volcano. The consistency between the two datasets supports the idea that the normalized chargeability field can be used to image alteration and temperature in stratovolcanoes.

A third point to discuss is the type of dominant clay minerals found in stratovolcanoes. For stratovolcanoes, deep ground waters are characterized by acidic conditions and kaolinite may dominate the clay members during the process of alteration through the leaching with these ground waters. Kaolinite has a CEC that is much smaller than smectite (5 meq/100 g versus 80–120 meq/100 g and therefore smaller surface conductivity). Mazot et al. (2008) found the presence of kaolinite in the rock samples from Papandayan but little evidence for smectite. Fig. 25 shows the conductivity distribution obtained from a magnetotelluric survey from Raguenel et al. (2019). Induced polarization can be used to better interpret such tomograms in terms of temperature, water content, CEC, and permeability distributions.

The fourth point to discuss concerns the way the normalized chargeability is computed. We first fit the complex conductivity spectra of the core samples from La Soufrière volcano using the double Cole Cole model discussed in Section 2.2 above (see also Tartrat et al., 2019). The fit are shown in Fig. 26 for the in-phase and quadrature components of the complex conductivity. The Cole Cole parameters are reported in Table 4. A comparison between Cole-Cole normalized chargeability (from Table 4, Low Frequency component) versus the quadrature conductivity at 32 Hz (see Table 3) for the samples from La Soufrière stratovolcano is shown in Fig. 27a. As predicted by Revil et al. (2017c), the proportionality coefficient is around 8. In Fig. 27b, the low-frequency Cole-Cole normalized chargeability is plotted as a function of the partial normalized chargeability determined as the difference of the in-phase conductivity between 1 Hz and 1 kHz. The slope is around 1.7 again consistent with the prediction of the simple model developed in Revil et al. (2017c).

The last point to discuss is the relationship between the quadrature conductivity and the pore water conductivity. Literature data shows that the amplitude of the quadrature conductivity increases with the salinity of the pore water and a maximum sometimes observed at high salinities (Weller et al., 2015). In Figs. 5b, d, we observe that the magnitude of the quadrature conductivity increases with the salinity by less than an order of magnitude for a change in two orders of magnitude in the pore water conductivity. This evolution can be explained by an electrical double layer model combined to a speciation model of the pore water / minerals

interface (Revil and Skold, 2011). It is however out of the scope of the present paper to explore in details such an effect, which would require the development of a simple double layer/speciation model associated with the mineral assemblage of andesitic rocks.

6. Conclusions

The present study leads to the following conclusions:

(1) The electrical properties of volcanic rocks from stratovolcanoes are similar to those of shield volcanoes. Once magnetite has disappeared, the in-phase and quadrature conductivities are controlled by the degree of alteration, itself associated with the presence of smectite at least as long as the pore water is relatively fresh and the pH near neutral conditions. Locally, the presence of pyrite can increase the quadrature conductivity and the normalized chargeability of the rocks. In stratovolcanoes, the presence of very acidic fluids can enhance the alteration of volcanic rocks. The salinity of the pore water and its pH are strongly related to each other but some exceptions could exist. In these conditions, above a pore water conductivity above 10 S m^{-1}, the bulk conductivity dominates the surface conductivity.

(2) The high conductivity of the altered rocks in la Soufrière and Papandayan stratovolcanoes is partly associated with alteration rather than associated with the high ionic strength of the pore water of the acidic hydrothermal fluids. This is shown from the laboratory core data analysis as well using the field data for the Papandayan study. The induced polarization survey performed at Papandayan volcano in Java Island confirms that the conductivity response is mostly the result of alteration with however a non-negligible contribution from the acidic pore water. The assumption made in previous works that surface conductivity could be neglected is not correct except perhaps when the salinity is close to saturation (TDS ~40,000 ppm and pH ~0.3).

(3) The tomography of the normalized chargeability can be used to assess the temperature distribution / altered areas associated with the upwelling of the acidic pore waters. A 3D temperature tomogram of Papandayan is produced and compared to surface data.

CRediT authorship contribution statement

A. Revil: Methodology, Writing – original draft, Conceptualization, Formal analysis, Project administration, Data curation, Supervision. **Y. Qi:** Investigation, Writing – original draft. **N. Panwar:** Investigation, Writing – original draft. **M. Gresse:** Investigation, Writing – original draft. **H. Grandis:** Investigation, Writing – original draft, Project administration. **R. Sharma:** Writing – review & editing. **Y. Géraud:** Investigation, Writing – original draft, Project administration. **N. Chibati:** Investigation, Writing – original draft. **A. Ghorbani:** Investigation, Writing – original draft.

Declaration of Competing Interest

The authors declare that they have no known competing financial interests or personal relationships that could have appeared to influence the work reported in this paper.

Acknowledgements

We thank the CNRS for supporting this work. Sampling and some petrophysical characterization of the Soufrière volcano are supported by the Geotref program. We acknowledge the Volcanological Survey of Indonesia (PVMBG) for permission to conduct the survey. We thank Egon Zimmermann for the construction of two ZEL- SIP04-V02 high precision impedance meters used for our laboratory experiments. *The data underlying this article will be shared on reasonable request to the corresponding author. We deeply thank the two first referees, Andreas Weller and Konstantin Titov, for a review of a first version of this work. We thank the Editors,* Alessandro Aiuppa and Tobias P. Fischer, an anonymous referee, and Craig Miller for their constructive comments of the second version of the manuscript.

References

Abdel Aal, G.Z., Atekwana, E.A., 2014. Spectral induced polarization (SIP) response of biodegraded oil in porous media. Geophys. J. Int. 196 (2), 804–817. https://doi.org/10.1093/gji/ggt416.

Abidin, H.Z., Andreas, H., Gamal, M., Sugandar, O.K., Meilano, I., Hendrasto, M., Kusuma, M.A., Darmawan, D., Purbawinata, M.A., Wirakusumah, A.D., Kimata, F., 2003. Ground deformation during Papandayan volcano 2002 eruption as detected by GPS surveys. Journal of Engineering and Technological Sciences 35 (1), 47–60. https://doi.org/10.5614/itbj.eng.sci.2003.35.1.4.

Aran, D., Maul, A., Masfaraud, J., 2008. A spectrophotometric measurement of soil cation exchange capacity based on cobaltihexamine chloride absorbance. Compt. Rendus Geosci. 340 (12), 865–871. https://doi.org/10.1016/j.crte.2008.07.015.

Archie, G.E., 1942. The electrical resistivity log as an aid in determining some reservoir characteristics. Trans. AIME 146, 54–62. https://doi.org/10.2118/942054-G.

Asmoro, P., Wachyudin, D., Mulyadi, E., 1989. Geological Map of Papandayan Volcano, Garut, West Java, Scale 1:25.000. Volcanological Survey of Indonesia.

Ball, J.L., Taron, J., Reid, M.E., Hurwitz, S., Finn, C., Bedrosian, P., 2018. Combining Multiphase Groundwater Flow and Slope Stability Models to Assess Stratovolcano Flank Collapse in the Cascade Range. Journal of Geophysical Research: Solid Earth 123 (4), 2787–2805. https://doi.org/10.1002/2017JB015156.

Bani, P., Hendrasto, M., Gunawan, H., Primulyana, S., 2013. Sulfur dioxide emissions from Papandayan and Bromo, two Indonesian volcanoes. Nat. Hazards Earth Syst. Sci. 13 (10), 2399–2407. https://doi.org/10.5194/nhess-13-2399-2013.

Békési, E., Struijk, M., Bonte, D., Veldkamp, J.G., Limberger, J., Fokker, P., Vrijlandt, M., Van Wees, J., 2020. An updated geothermal model of the Dutch subsurface based on inversion of temperature data. Geothermics 88, 101880. https://doi.org/10.1016/j.geothermics.2020.101880.

Bernabé, Y., Revil, A., 1995. Pore-scale heterogeneity, energy dissipation and the transport properties of rocks. Geophys. Res. Lett. 22 (12), 1529–1552. https://doi.org/10.1029/95GL01418.

Binley, A., Hubbard, S.S., Huisman, J.A., Revil, A., Robinson, D.A., Singha, K., Slater, L. D., 2015. The emergence of hydrogeophysics for improved understanding of subsurface processes over multiple scales. Water Resour. Res. 51, 3837–3866. https://doi.org/10.1002/2015WR017016.

Börner, F.D., Gruhne, M., Schön, J.H., 1993. Contamination indications derived from electrical properties in the low frequency range. Geophys. Prospect. 41, 83–98.

Broyden, C.G., 1965. A class of methods for solving nonlinear simultaneous equations. Math. Comput. 19 (92), 577–593.

Brunauer, S., Emmett, P.H., Teller, E., 1938. Adsorption of gasses in multimolecular layers. Journal of American Chemical Society 60 (2), 309–319. https://doi.org/10.1021/ja01269a023.

Bussian, A.E., 1983. Electrical conductance in a porous medium. Geophysics 48, 1258–1268.

Byrdina, S., Grandis, H., Sumintadireja, P., Caudron, C., Syahbana, D.K., Naffrechoux, E., Gunawan, H., Suantika, G., Vandemeulebrouck, J., 2018. Structure of the acid hydrothermal system of Papandayan volcano, Indonesia, investigated by geophysical methods. J. Volcanol. Geotherm. Res. 358, 77–86.

Carracedo, J.C., Troll, V.R., 2013. Teide Volcano: Geology and Eruptions of a Highly Differentiated Oceanic Stratovolcano. Active Volcanoes of the World. Springer-Verlag, Berlin Heidelberg.

Dianardi, K., Jumhari, Hadian M.S.D., Iskandarsyah, T.Y.M., 2018. Characteristics of groundwater on the Eastern slope of Mount Ciremai, Kuningan Regency, West Java, Indonesia. Journal of Geoscience, Engineering, Environment, and Technology 3 (04). https://doi.org/10.24273/jgeet.2018.3.4.1606.

Finizola, A., Revil, A., Rizzo, E., Piscitelli, S., Ricci, T., Morin, J., Angeletti, B., Mocochain, L., Sortino, F., 2006. Hydrogeological insights at Stromboli volcano (Italy) from geoelectrical, temperature, and CO_2 soil degassing investigations. Geophys. Res. Lett. 33, L17304. https://doi.org/10.1029/2006GL026842.

Finn, C.A., Sisson, T.W., Deszcz-Pan, M., 2001. Aerogeophysical measurements of collapse prone hydrothermally altered zones at Mount Rainier volcano. Nature 409 (6820), 600. https://doi.org/10.1038/35054533.

Flores Orozco, A., Velimirovic, M., Tosco, T., Kemna, A., Sapion, H., Klaas, N., Sethi, R., Bastiaens, L., 2015. Monitoring the injection of microscale zerovalent iron particles for groundwater remediation by means of complex electrical conductivity imaging. Environ. Sci. Technol. 49 (9), 5593–5600.

Flóvenz, O.G., 2005. The Role of Electrical Interface Conduction in Geothermal Exploration Proceedings World Geothermal Congress 2005, Antalya, Turkey, 24–29 April 2005.

Fujii, M., Sato, H., Shimada, K., Ishibashi, J.-I., 2018. Seafloor hydrothermal alteration affecting magnetic properties of abyssal basaltic rocks: insights from back-arc lavas of the Okinawa Trough. Earth, Planets and Space 70, 196. https://doi.org/10.1186/s40623-018-0958-6.

Ghorbani, A., Revil, A., Coperey, A., Soueid, Ahmed A., Roque, S., Heap, M.J., Grandis, H., Viveiros, F., 2018. Complex conductivity of volcanic rocks and the

geophysical mapping of alteration in volcanoes. J. Volcanol. Geotherm. Res. 357, 106–127. https://doi.org/10.1016/j.jvolgeores.2018.04.014.
Gresse, M., Uyeshima, M., Koyama, T., Hase, H., Aizawa, K., Yamaya, Y., Hata, M., 2021. Hydrothermal and magmatic system of a volcanic island inferred from magnetotellurics, seismicity, self-potential, and thermal image: an example of Miyakejima (Japan). Journal of Geophysical Research: Solid Earth 126 (6). https://doi.org/10.1029/2021JB022034 e2021JB022034.
Gross, L., Soueid, Ahmed A., Revil, A., 2021. Induced polarization of volcanic rocks. 4. Large-scale induced polarization imaging. Geophys. J. Int. 225 (2), 950–967. https://doi.org/10.1093/gji/ggab018.
Hadisantono, R.D., 2006. Devastating landslides related to the 2002 Papandayan eruption. Indonesian Journal on Geoscience 1 (2), 83–88. https://doi.org/10.17014/ijog.1.2.83-88.
Hasan, M.M., Triastuty, H., Santosa, B.J., Widodo, A., 2016. Hypocenter distribution of low frequency event at Papandayan volcano. Journal Neutrino 9 (1), 10–14. https://doi.org/10.18860/neu.v9i1.3655.
Janssen, V., Roberts, C., Rizos, C., Abidin, H.Z., 2002. Low-cost GPS-based volcano deformation monitoring at Mt. Papandayan, Indonesia. J. Volcanol. Geotherm. Res. 115 (1–2), 139–151.
Johnson, T.C., Versteeg, R.J., Ward, A., Day-Lewis, F.D., Revil, A., 2010. Improved hydrogeophysical characterization and monitoring through parallel modeling and inversion of time-domain resistivity and induced-polarization data. Geophysics 75. https://doi.org/10.1190/1.3475513 (WA27–WA41).
Joseph, E.P., Fournier, N., Lindsay, J.M., Robertson, R., Beckles, D.M., 2013. Chemical and isotopic characteristics of geothermal fluids from Sulphur Springs, Saint Lucia. J. Volcanol. Geotherm. Res. 254, 23–36.
Jougnot, D., Ghorbani, A., Revil, A., Leroy, P., Cosenza, P., 2010. Spectral Induced Polarization of partially saturated clay-rocks: A mechanistic approach. Geophys. J. Int. 180 (1), 210–224. https://doi.org/10.1111/j.1365-246X.2009.04426.x.
Kedar, S., Panning, M., Smrekar, S., Stähler, S., King, S., Golombek, M., Manga, M., Julian, B., Shiro, B., Perrin, C., Power, J., Michaut, C., Ceylan, S., Giardini, D., Lognonné, P., Banerdt, W., 2021. Analyzing Low Frequency Seismic events at Cerberus Fossae as Long Period Volcanic Quakes. Journal of Geophysical Research: Planets 126. https://doi.org/10.1029/2020JE006518.
Kemna, A., 2000. Tomographic Inversion of Complex Resistivity: Theory and Application. PhD thesis. Bochum University (196pp).
Kristmannsdóttir, H., 1979. Alteration of basaltic rocks by hydrothermal activity at 100–300°C. In: Mortland, M.M., Farmer, V.C. (Eds.), International Clay Conference 1978. Elsevier Scientific Publishing Co., Amsterdam, pp. 359–367.
Leroy, P., Revil, A., Kemna, A., Cosenza, P., Ghorbani, A., 2008. Complex conductivity of water-saturated packs of glass beads. J. Colloid Interface Sci. 321 (1), 103–117. https://doi.org/10.1016/j.jcis.2007.12.031.
Lesmes, D.P., Morgan, F.D., 2001. Dielectric spectroscopy of sedimentary rocks. J. Geophys. Res. 106 (B7) (13 329–13 346).
Liotta, D., Brogi, A., Ruggieri, G., Rimondi, V., Zucchi, M., Helgadóttir, H.M., Montegrossi, G., Friðleifsson, G.O., 2020. Fracture analysis, hydrothermal mineralization and fluid pathways in the Neogene Geitafell central volcano: insights for the Krafla active geothermal system, Iceland Domenico. Journal of Volcanology and Geothermal Research. https://doi.org/10.1016/j.jvolgeores.2018.11.023.
López, D.L., Williams, S.N., 1993. Catastrophic volcanic collapse: relation to hydrothermal processes. Science. 260 (5115), 1794–1796. https://doi.org/10.1126/science.260.5115.1794.
Lyklema, J., 2002. The role of surface conduction in the development of electrokinetics. In: Interfacial Electrokinetics and Electrophoresis, 106. A.V. Delgado, pp. 87–97. Surfact. Sci. Ser. (991pp).
Mannen, K., Tanada, T., Jomori, A., Akatsuka, T., Kikugawa, G., Fukazawa, Y., Yamashita, H., Fujimoto, K., 2019. Source constraints for the 2015 phreatic eruption of Hakone volcano, Japan, based on geological analysis and resistivity structure. Earth, Planets and Space 71. https://doi.org/10.1186/s40623-019-1116-5.
Matoza, R.S., Chouet, B.A., 2010. Subevents of long-period seismicity: Implications for hydrothermal dynamics during the 2004–2008 eruption of Mount St. Helens. Journal of Geophysical Research: Solid Earth 115 (B12). https://doi.org/10.1029/2010JB007839.
Mazot, A., 2005. Activité hydrothermale des volcans Kelud et Papandayan (Indonésie) et évaluation des flux de gaz carbonique. PhD Thesis. Université Libre de Bruxelles (294 pp.).
Mazot, A., Bernard, A., Fischer, T., Inguaggiato, S., Sutawidjaja, I.S., 2008. Chemical evolution of thermal waters and changes in the hydrothermal system of Papandayan volcano (West Java, Indonesia) after the November 2002 eruption. J. Volcanol. Geotherm. Res. 178 (2), 276–286.
Muñoz, G., 2014. Exploring for geothermal resources with electromagnetic methods. Survey in Geophysics 35, 101–122. https://doi.org/10.1007/s10712-013-9236-0.
Muñoz, G., Ritter, O., Moeck, I., 2010a. A target-oriented magnetotelluric inversion approach for characterizing the low enthalpy Groß Schönebeck geothermal reservoir. Geophys. J. Int. 183, 1199–1215.
Muñoz, G., Bauer, K., Moeck, I., Schulze, A., Ritter, O., 2010b. Exploring the Groß Schönebeck (Germany) geothermal site using a statistical joint interpretation of magnetotelluric and seismic tomography models. Geothermics 39, 35–45.
Nasution, A., Widarto, D.S., Hutasoit, L., Yuliani, D., Hadisoemarto, S., 2008. Geothermal geophysical study of Mt. Papandayan, Garut District, West Java Indonesia. In: Proceedings of the 8th Asian Geothermal Symposium.
Navelot, V., 2018. Caractérisations structurale et pétrophysique d'un système géothermique en contexte volcanique d'arc de subduction Exemple de l'archipel de Guadeloupe. PhD Thesis. Université de Lorraine (440 p).
Navelot, V., Géraud, Y., Favier, A., Diraison, M., Corsini, M., Lardeaux, J.-M., Verati, C., Mercier de Lépinay, J., Legendre, L., Beauchamps, G., 2018. Petrophysical properties of volcanic rocks and impacts of hydrothermal alteration in the Guadeloupe Archipelago (West Indies). J. Volcanol. Geotherm. Res. 360, 1–21. https://doi.org/10.1016/j.jvolgeores.2018.07.004.
Niu, Q., Revil, A., Saidian, M., 2016. Salinity dependence of the complex surface conductivity of the Portland sandstone. Geophysics 81 (2), D125–D140. https://doi.org/10.1190/GEO2015-0426.1.
Nurhasan, S., Srigutomo, W., Viridi, S., Fitriani, D., 2012. Integrated geophysical measurements for subsurface mapping at Papandayan volcano, Garut, Indonesia (preliminary result). In: American Institute of Physics Conference Series, 1454(1), pp. 154–157.
Ohminato, T., 2006. Characteristics and source modeling of broadband seismic signals associated with the hydrothermal system at Satsuma–Iwojima volcano, Japan. J. Volcanol. Geotherm. Res. 158 (3), 467–490. https://doi.org/10.1016/j.jvolgeores.2006.08.004.
Oldenburg, D.W., Li, Y., 1994. Inversion of induced polarization data. Geophysics 59 (9), 1327–1341.
Olhoeft, G.R., 1985. Low-frequency electrical properties. Geophysics 50 (12), 2492–2503. https://doi.org/10.1190/1.1441880.
Oliva-Urcia, B., Kontny, A., Carsten, V., Schleicher, A.M., 2011. Modification of the magnetic mineralogy in basalts due to fluid–rock interactions in a high-temperature geothermal system (Krafla, Iceland). Geophys. J. Int. 186 (1), 155174 https://doi.org/10.1111/j.1365-246X.2011.05029.x.
Qi, Y., Soueid, A., Revil, A., Ghorbani, A., Abdulsamad, F., Florsch, N., Bonnenfant, J., 2018. Induced polarization response of porous media with metallic particles—part 7: Detection and quantification of buried slag heaps. Geophysics 83, E277–E291.
Qi, Y., El-Kaliouby, H., Revil, A., Soueid Ahmed, A., Ghorbani, A., Li, J., 2019. Three-dimensional modeling of frequency- and time-domain electromagnetic methods with induced polarization effects. Comput. Geosci. 124 (3), 85–92. https://doi.org/10.1016/j.cageo.2018.12.011.
Raguenel, M., Driesner, T., Bonneau, F., 2019. Numerical modeling of the geothermal hydrology of the Volcanic Island of Basse-Terre, Guadeloupe. Geothermal Energy 7, 28. https://doi.org/10.1186/s40517-019-0144-5.
Reid, M.E., 2004. Massive collapse of volcano edifices triggered by hydrothermal pressurization. Geology 32 (5), 373–376. https://doi.org/10.1130/G20300.1.
Revil, A., Cathles, L.M., 1999. Permeability of shaly sands. Water Resour. Res. 35 (3), 651–662.
Revil, A., Skold, M., 2011. Salinity dependence of spectral induced polarization in sands and sandstones. Geophys. J. Int. 187, 813–824. https://doi.org/10.1111/j.1365-246X.2011.05181.x.
Revil, A., Hermitte, D., Spangenberg, E., Cochémé, J.J., 2002. Electrical properties of zeolitized volcaniclastic materials. J. Geophys. Res. 107 (B8), 2168. https://doi.org/10.1029/2001JB000599.
Revil, A., Le Breton, M., Niu, Q., Wallin, E., Haskins, E., Thomas, D.M., 2017a. Induced polarization of volcanic rocks. 1. Surface versus quadrature conductivity. Geophys. J. Int. 208, 826–844. https://doi.org/10.1093/gji/ggw444.
Revil, A., Le Breton, M., Niu, Q., Wallin, E., Haskins, E., Thomas, D.M., 2017b. Induced polarization of volcanic rocks. 2. Influence of pore size and permeability. Geophys. J. Int. 208, 814–825. https://doi.org/10.1093/gji/ggw382.
Revil, A., Coperey, A., Shao, Z., Florsch, N., Fabricius, I.L., Deng, Y., Delsman, J.R., Pauw, P.S., Karaoulis, M., de Louw, P.G.B., van Baaren, E.S., Dabekaussen, W., Menkovic, A., Gunnink, J.L., 2017c. Complex conductivity of soils. Water Resour. Res. 53 (8), 7121–7147. https://doi.org/10.1002/2017WR020655.
Revil, A., Qi, Y., Ghorbani, A., Soueid, A., Ricci, T., Labazuy, P., 2018. Electrical conductivity and induced polarization investigations at Krafla volcano, Iceland. J. Volcanol. Geotherm. Res. 368, 73–90. https://doi.org/10.1016/j.jvolgeores.2018.11.008.
Revil, A., Qi, Y., Ghorbani, A., Coperey, A., Soueid, A., Finizola, A., Ricci, T., 2019. Induced polarization of volcanic rocks. 3. Imaging clay cap properties in geothermal fields. Geophys. J. Int. 218 (2), 1398–1427. https://doi.org/10.1093/gji/ggz207.
Revil, A., Coperey, A., Heap, M.J., Carbillet, L., 2020. A geophysical index to map alteration, permeability, and mechanical properties within volcanoes. Application to the soft volcanic rocks from Whakaari/White Island (New Zealand). J. Volcanol. Geotherm. Res. 401, 106945 https://doi.org/10.1016/j.jvolgeores.2020.106945.
Revil, A., Qi, Y., Ghorbani, A., Gresse, M., Thomas, D.M., 2021. Induced polarization of volcanic rocks. 5. Imaging the temperature field of shield volcanoes. Geophys. J. Int. 225, 1492–1509. https://doi.org/10.1093/gji/ggab039.
Revil, A., Vaudelet, P., Su, Z., Chen, R., 2022. Induced polarization as a tool to assess mineral deposits: a review. Minerals 12, 571. https://doi.org/10.3390/min12050571.
Rosas-Carbajal, M., Komorowski, C., Nicollin, J.C., Gibert, D., 2016. Volcano electrical tomography unveils edifice collapse hazard linked to hydrothermal system structure and dynamics. Science Report. 6, 29899. https://doi.org/10.1038/srep29899.
Salaun, A., Villemant, B., Gerard, M., Komorowski, J.-C., 2011. A. Hydrothermal alteration in andesitic volcanoes: trace element redistribution in active and ancient hydrothermal systems of Guadeloupe (Lesser Antilles). J. Geochem. Explor. 111, 59–83.
Samper, A., Quidelleur, X., Komorowski, J.-C., Lahitte, P., Boudon, G., 2009. Effusive history of the Grande Découverte Volcanic Complex, southern Basse-Terre (Guadeloupe, French West Indies) from new K–Ar Cassignol–Gillot ages. J. Volcanol. Geotherm. Res. 187, 117–130. https://doi.org/10.1016/j.jvolgeores.2009.08.016.
Sassa, K., Dang, K., Yanagisawa, H., He, B., 2016. A new landslide-induced tsunami simulation model and its application to the 1792 Unzen-Mayuyama landslide-and-tsunami disaster. Landslides 13, 1405–1419. https://doi.org/10.1007/s10346-016-0691-9.
Schlumberger, C., 1920. Etude Sur la prospection électrique du sous-sol. Gauthier-Villars, Paris. The second edition without modification is available at.

Schmutz, M., Albouy, Y., Guérin, R., Maquaire, O., Vassal, J., Schott, J., Descloitres, M., 2000. Joint inversion applied to the Super Sauze earthflow (France). Surv. Geophys. 21 (4), 371–390.

Soueid Ahmed, A., Revil, A., Byrdina, S., Coperey, A., Gailler, L., Grobbe, N., Viveiros, F., Jougnot, D., Ghorbani, A., Hogg, C., Kiyan, D., Rath, V., Heap, M.J., Grandis, H., Humaida, H., 2018. 3D electrical conductivity tomography of volcanoes. J. Volcanol. Geotherm. Res. 356 (243–263), 2018. https://doi.org/10.1016/j.jvolgeores.2018.03.017.

Stimac, J., Goff, F., Goff, C.J., 2015. Chapter 46 - intrusion-related geothermal systems. In: Sigurdsson, H. (Ed.), The Encyclopedia of Volcanoes (Second Edition), 799–822. Academic Press, Amsterdam. https://doi.org/10.1016/B978-0-12-385938-9.00046-8.

Syahbana, D.K., Caudron, C., Jousset, P., Lecocq, T., Camelbeeck, T., Bernard, A., 2014. Fluid dynamics inside a "wet" volcano inferred from the complex frequencies of long-period (LP) events: an example from Papandayan volcano, West Java, Indonesia, during the 2011 seismic unrest. J. Volcanol. Geotherm. Res. 280, 76–89.

Tartrat, T., Revil, A., Abdulsamad, F., Ghorbani, A., Jougnot, D., Coperey, A., Yven, B., de la Vaissière, R., 2019. Induced polarization response of porous media with metallic particles – Part 10. Influence of desiccation. Geophysics 84 (5), E357–E375. https://doi.org/10.1190/geo2019-0048.1.

Titov, K., Komarov, V., Tarasov, V., Levitski, A., 2002. Theoretical and experimental study of time domain-induced polarization in water-saturated sands. J. Appl. Geophys. 50, 417–433. https://doi.org/10.1016/S0926-9851(02)00168-4.

Triastuty, H., Iguchi, M., Tameguri, T., 2006. Source mechanism of monochromatic and low-frequency events at Papandayan Volcano, West Java, Indonesia. Indonesian Journal of Physics 17 (3), 63–71.

van Olphen, H., 1957. Surface conductance of various ion forms of bentonite in water and the electrical double layer. J. Phys. Chem. 61, 1276–1280.

van Olphen, H., Waxman, M.H., 1958. Surface conductance of sodium bentonite in water. Clay Clay Miner. 5 (1), 61–80.

Vinegar, H., Waxman, M., 1984. Induced polarization of shaly sands. Geophysics 49 (8), 1267–1287. https://doi.org/10.1190/1.1441755.

Watt, S.F.L., Talling, P.J., Vardy, M.E., Heller, V., Hühnerbach, V., Urlaub Sarkar, M., Masson, S.D.G., Henstock, T.J., Minshull, T.A., Paulatto, M., Le Friant, A., Lebas, E., Berndt, C., Crutchley, G.J., Karstens, J., Stinton, A.J., Maeno, F., 2012. Combinations of volcanic-flank and seafloor sediment failure offshore Montserrat, and their implications for tsunami generation. Earth Planetary Science Letters 319–320, 228–240.

Watters, R.J., Zimbelman, D.R., Bowman, S.D., Crowley, J.K., 2000. Rock mass strength assessment and significance to edifice stability, Mount Rainier and Mount Hood, Cascade Range volcanoes. Pure Appl. Geophys. 157, 957–976.

Waxman, M.H., Smits, L.J.M., 1968. Electrical conductivities in oil bearing shaly sands. Society of Petroleum Engineers Journal 8, 107–122. https://doi.org/10.2118/1863-A.

Weller, A., Slater, L., Nordsiek, S., 2013. On the relationship between induced polarization and surface conductivity: Implications for petrophysical interpretation of electrical measurements. Geophysics 78, D315–D325. https://doi.org/10.1190/GEO2013-0076.

Weller, A., Zhang, Z., Slater, L., 2015. High-salinity polarization of sandstones. Geophysics 80 (3), D309–D318. https://doi.org/10.1190/geo2014-0483.1.

Zimmermann, E., Kemna, A., Berwix, J., Glaas, W., Münch, H.M., Huisman, J.A., 2008. A high-accuracy impedance spectrometer for measuring sediments with low polarizability. Meas. Sci. Technol. 19 (10), 105603 https://doi.org/10.1088/0957-0233/19/10/105603.

Zimmermann, E., Huisman, J.A., Mester, A., van Waasen, S., 2019. Correction of phase errors due to leakage currents in wideband EIT field measurements on soil and sediments. Meas. Sci. Technol. 30 (8), 084002.

Zukoski, C.F., Saville, D.A., 1986a. The interpretation of electrokinetic measurements using a dynamic model of the stern layer. I. the dynamic model. Journal of Colloid. Interface Science 114 (1), 32–44.

Zukoski, C.F., Saville, D.A., 1986b. The interpretation of electrokinetic measurements using a dynamic model of the stern layer. II. Comparisons between theory and experiments. Journal of Colloid Interface Science 114 (1), 45–53.